APPROACHES FOR IMPROVED PRECISION OF MICROWAVE THERMAL THERAPY

by

BROGAN MCWILLIAMS

B.S., Kansas State of University, 2012

A THESIS

submitted in partial fulfillment of the requirements for the degree

MASTER OF SCIENCE

Department of Electrical and Computer Engineering
College of Engineering

KANSAS STATE UNIVERSITY
Manhattan, Kansas

2015

Approved by:

Major Professor
Dr. Punit Prakash

Copyright

Abstract

Thermal therapies employing interstitial microwave applicators for hyperthermia or ablation are in clinical use for treatment of cancer and benign disease in various organs. However, treatment of targets in proximity to critical structures with currently available devices is risky due to unfocused deposition of energy into tissue. For successful treatment, complete thermal coverage of the tumor and margin of surrounding healthy tissue must be achieved, while precluding damage to critical structures. This thesis investigates two approaches to increase precision of microwave thermal therapy. Chapter 2 investigates a novel coaxial antenna design for microwave ablation (MWA) employing a hemi-cylinderical reflector to achieve a directional heating pattern. A proof of concept antenna with an S_{11} of -29 dB at 2.45 GHz was used in *ex vivo* experiments to characterize the antennas' heating pattern with varying input power and geometry of the reflector. Ablation zones up to 20 mm radially were observed in the forward direction, with minimal heating (less than 4 mm) behind the reflector. Chapter 3 investigates the use of magnetic nanoparticles (MNP) of varying size and geometry for enhancing microwave tissue heating. A conventional dipole, operating at 2.45 GHz and radiating 15 W, was inserted into a 20 mm radius sphere of distributed MNPs and heating measurements were taken 5 mm, 10 mm, and 15 mm radially away. A heating rate of 0.08 °C/s was observed at 10 mm, an increase of 2-4 times that of the control measurement. These approaches provide strong potential for improving spatial control of tissue heating with interstitial and catheter-based microwave antennas.

Table of Contents

List of Figures

List of Tables

Acknowledgements

I would like to acknowledge several students and colleagues who have assisted me in acquiring and interpreting the data this thesis is create around. I would like to acknowledge and thank Emily Schnell and Valerie Binns for helping me with my work on the evaluation of the directional antenna and characterization of the thermal properties of MNPs at microwave frequencies. I also like to thank Sergio Curto and Hongwang Wang for their participation and expertise in their respective fields.

I would like to thank my committee members Dr. William Kuhn, Dr. Stefan Bossmann, and Dr. Punit Prakash for reviewing and helping me to improve this document. I especially like to thank Dr. Punit Prakash for being my major professor, an advisor for me during my Masters', and for the guidance on my future career.

Dedication

I dedicate this thesis to my parents and brother, without them I would have not have been instilled with the determination to achieve my goals.

Chapter 1 - Introduction

Thermal therapy is the process of heating biological tissue to cause cell damage or death for the treatment of disease and requires the implementation of various systems that must work in conjecture as shown in figure 1.1. Various energy delivery modalities for thermal therapies have been designed and used as a stand-alone procedure for the treatment of tumors to reduce invasiveness of surgeries and in parallel with current standard clinical procedures to increase the effectiveness of the treatment. Hyperthermia is used adjuvant to radiation therapy and/or chemotherapy for cancer treatment; in hyperthermia procedures, the targeted region of tissue is heated to temperatures in the range of 41-43°C, thereby enhancing the efficacy of radiation therapy, chemotherapy, and inducing a mild anti-tumor immune response [1]. Heating above 45 °C may result in irreversible cell damage, while heating above 60 °C leads to near instantaneous cell death and results in ablation (*i.e.* irreversible thermal tissue destruction)[2].

Figure 1.1: Block Diagram of Thermal Therapy System (model of body taken from [3])

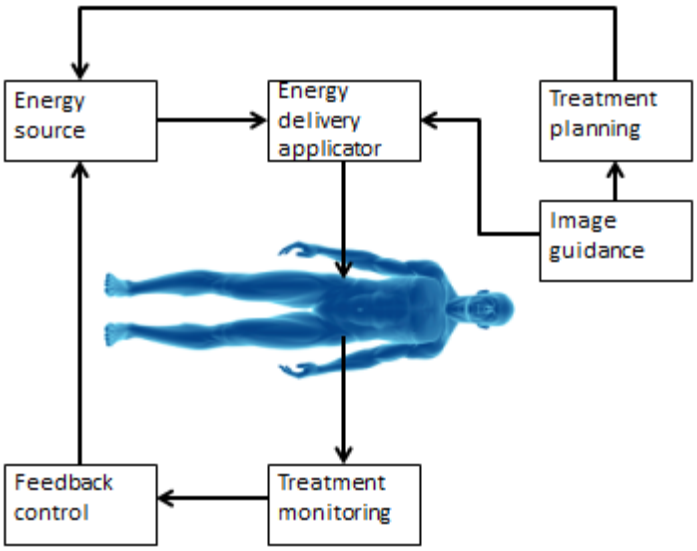

Cell death due to thermal ablation has been shown to be a complex function of time of exposure and temperature, which can be predicted using a dimensionless damage parameter Ω (eq.1) determined from an Arrhenius rate-of-formation kinetic model [4].

$$\boldsymbol{\Omega(\tau) = \int_0^{\tau} A e^{\left[\frac{-E_a}{RT(\tau)}\right]} dt} \tag{1.1}$$

Where A is known as the "frequency factor" (s^{-1}), E_a is an energy barrier ($Jmole^{-1}$), R is the gas constant (8.3143 $Jmole^{-1}K^{-1}$), T is temperature (K), and τ is total experimental time (s). The thermal dosage modeled by Ω shows various approaches to achieving cell death by fluctuating therapy time and the associated temperature rise to achieve a certain percentage of damaged tissue to healthy tissue (eq.2).

$$\boldsymbol{P = 100[1 - e^{-\Omega}]} \tag{1.2}$$

High intensity focused and catheter based ultrasound (US) [5],[6], chemical [7], radiofrequency (RF) [8], laser [9], thermal conduction [10], and microwave (MW) have been investigated modalities for delivery of energy during hyperthermia and ablation procedures. High intensity focused ultrasound is performed non-invasively and has high precision but regions of air such as bone and lungs oppose penetration of ultrasound and can result in unintended heating in regions near these structures. Furthermore, noninvasive ablation is currently faced with the problems of time duration of the procedure, accurate thermometry, and accurate lesion production monitoring to ensure adequate ablation of the region of interest [11]. Due to the minimally invasive nature of catheter based modalities, it has been investigated as a faster and less expensive procedure for ablation. Microwave ablation offers deeper tissue and scar penetration than RF due to an observed impedance increase exhibited after charring of tissue

[12]. Both RF and microwave are less invasive and able to be used for deeper seated tumors compare to conductive interstitial thermal therapy (CITT) [13]. Clinically microwave ablation is used in the treatment of cardiac arrhythmia [14], [15] and solid tumors under 3 cm radially located in the liver [16], bone [17], kidneys [18], and lungs[19].

Microwave energy is transmitted to the target tissue through coaxial based antennas, which are modified at the tip of the line to optimize radiation at certain frequencies, usually 433 MHz, 915 MHz, and 2.45 GHz. Conventional coaxial antennas can be classified as dipole, slot, or monopole and have cylindrically symmetric E-field patterns radiating 3-4 cm from the tip and afford limited control of spatial power deposition profiles [20] .These antennas are placed inside Teflon catheters with diameters less than 3 mm and water can be circulated in the catheter to maintain temperatures along the coaxial line. Figure 1.2 illustrates the specific absorption rate (SAR) profile of a cap choke antenna.

Figure 1.2: SAR distribution of Cap choke antenna(taken from [21])

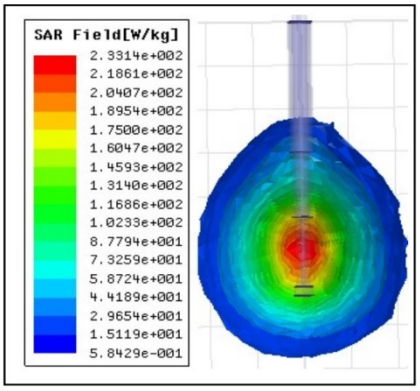

SAR is a measure of the rate of energy absorbed by biological tissue when exposed to a radiating energy and is dependent on tissue properties and field strength of the antenna. Electromagnetic (EM) waves in the microwave frequency range of 300 MHz to 300 GHz can be described by Maxwells' equations in differential form (eq.3-7).

$$\nabla \times \mathbf{H} = \mathbf{J_c} + \frac{\partial \mathbf{D}}{\partial \mathbf{t}} \tag{1.3}$$

$$\nabla \times \mathbf{E} = -\frac{\partial \mathbf{B}}{\partial \mathbf{t}} \tag{1.4}$$

$$\nabla \cdot \mathbf{D} = \boldsymbol{\rho} \tag{1.5}$$

$$\nabla \cdot \mathbf{B} = \mathbf{0} \tag{1.6}$$

Where **E** is the electrical field intensity [V/m], **B** is the magnetic field intensity [A/m], **D** is the electrical flux density [C/m^2], **H** is the magnetic flux density [Wb/m^2], $\boldsymbol{J_c}$ is the electric current density [A/m^2], and ρ is the volume charge density [C/m^3]. Furthermore, the **E** and **B** fields also satisfy the wave equation (eq.7-8) [22][21].

$$\nabla^2 \mathbf{E} - \boldsymbol{\varepsilon_r \varepsilon_0 \mu_r \mu_0} \frac{\partial^2 \mathbf{E}}{\partial \mathbf{t}^2} = \mathbf{0} \tag{1.7}$$

$$\nabla^2 \mathbf{B} - \boldsymbol{\varepsilon_r \varepsilon_0 \mu_r \mu_0} \frac{\partial^2 \mathbf{B}}{\partial \mathbf{t}^2} = \mathbf{0} \tag{1.8}$$

Where ε_r is relative permittivity, ε_0 [F/m] is the permittivity of free space, μ_r is relative permeability, μ_0 [V·s/A·m] is the permeability of free space.

The relative permittivity and permeability are properties of the medium through which the wave propagates. Both properties can be expressed as complex values (eq.9-10).

$$\boldsymbol{\varepsilon}^*(\mathbf{f}) = \boldsymbol{\varepsilon}'(\mathbf{f}) - \mathbf{j}\boldsymbol{\varepsilon}''(\mathbf{f}) \tag{1.9}$$

$$\boldsymbol{\mu}^*(\mathbf{f}) = \boldsymbol{\mu}'(\mathbf{f}) - \mathbf{j}\boldsymbol{\mu}''(\mathbf{f}) \tag{1.10}$$

ε' and μ' represent the energy stored in the medium from the **E** and **B**-field respectively . ε'' and μ'' represent the energy loss to the medium from the **E** and **B**-field respectively. ε'' can be related to the conductivity of the medium (eq.11) [22],[23], [24].

$$\varepsilon'' = \frac{\sigma}{\omega \varepsilon_o} \tag{1-11}$$

The values of ε^*, μ^*, and σ are dependent on the frequency of the EM wave. The relative permittivity and conductivity of human blood, bone (cancellous), muscle, and fat in the microwave frequency range are shown in figure 1.3 and1.4, μ' and μ'' are approximately 1 and 0 at microwave frequencies for biological tissues .

Figure 1.3: Relative permittivity vs frequency of biological tissues

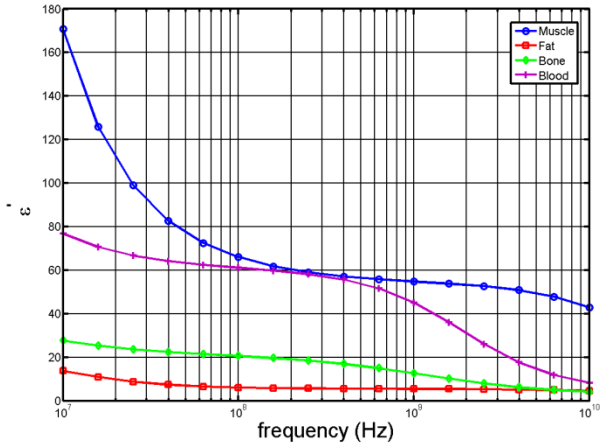

Figure 1.4: Conductivity vs frequency of biological tissues

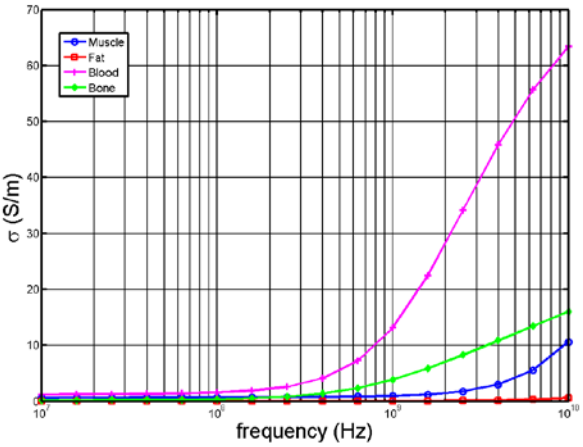

To describe fields within lossy dielectric and magnetic media the simplest solution is to assume a plane traveling sinusoidal wave of single frequency as illustrated by figure 1.5.

Figure 1.5: E and H field propagation through a lossy medium(taken from [24])

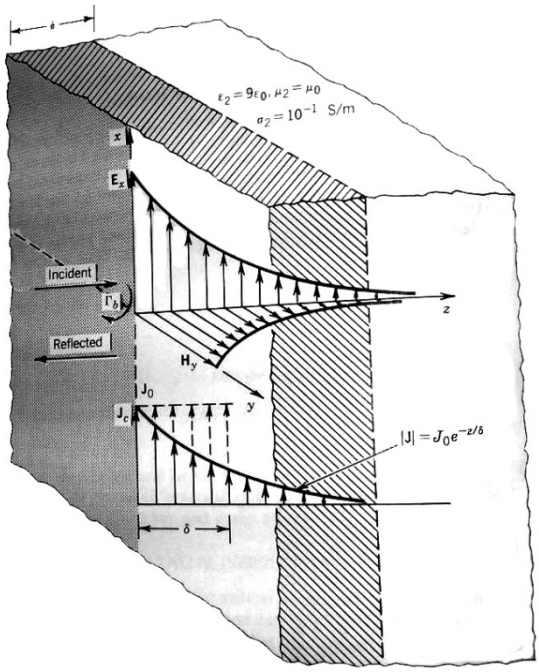

According to the Beer-Lambert law, the amplitude of an electromagnetic wave decreases exponentially as it propagates from the surface into a lossy medium [25].

$$\mathbf{E(r) = E_o e^{-\gamma r} \text{ or } B(r) = B_o e^{-\gamma r}} \tag{1.12}$$

With γ defined as the complex propagation constant (eq.13).

$$\boldsymbol{\gamma = \sqrt{j\omega\mu^*(\sigma + j\omega\varepsilon^*)} = \alpha + j\beta} \tag{1.13}$$

σ is the conductivity of the material in a static electric field, **ω** is the angular frequency (rad/s), α (Np m^{-1}) is the attenuation coefficient, the real part of the propagation constant, and quantifies how much attenuation an EM wave will experience as it propagates through a medium. The penetration depth, δ in figure 1.4, is defined as the distance into a medium over which an EM

field is reduced by a factor of $e^{-1} \approx 36.8\%$ and is the inverse of α. β (Radians m^{-1}) is the phase constant, the imaginary part of the propagation constant, and defines the wavelength of EM wave in a lossy medium (eq.14).

$$\boldsymbol{\lambda = \frac{2\pi}{\beta}} \tag{1.14}$$

As shown by equation 1.14 the wavelength is dependent on frequency and the electrical properties of the medium. The wavelength is an important measure for antenna design, with the antennas' geometric dimensions being related to an order of the wavelength. Higher frequencies result in smaller wavelengths as shown in figure 1.6 and can be taken advantage to reduce antenna dimensions.

Figure 1.6: wavelength vs frequency of biological tissues

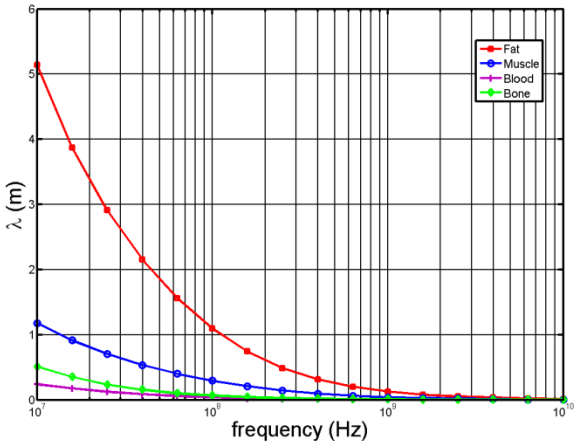

The energy associated to an EM wave and deposition of energy into tissue is described by the Poynting theorem [9].

$$-\frac{\partial u}{\partial t} = \frac{\partial}{\partial t}\int_V (\boldsymbol{\varepsilon}^* \mathbf{E}\cdot\mathbf{E} + \boldsymbol{\mu}^* \mathbf{H}\cdot\mathbf{H})\mathbf{dV} + \int_S (\mathbf{E}\times\mathbf{H})\cdot\mathbf{dS} \tag{1.15}$$

The volume integral represents the instantaneous total energy contained in the volume by the **E** and **H** field. The vector term $\boldsymbol{E}\times\boldsymbol{H}$ is defined as the Poynting vector with the surface integral representing the total power passing through the closed surface. The left hand side of the

equations represents the time rate of change of stored energy (Joules/s) inside V. For sinusoidal fields, the time-averaged energy stored in the electric and magnetic field is zero. Therefore, using time averaged values for equation 15 the following can be determined.

$$-\int_{\mathbf{S}}\langle \mathbf{P}\rangle \, \mathbf{dS} = \int_{\mathbf{V}}\langle \boldsymbol{Q_{gen}}\rangle \mathbf{dV} \tag{1.16}$$

Where **P** is the total average power passing into or out of the volume through the surface S, Q_{gen} is the total average power transferred to the charged particles within the field. For steady state sinusoidal fields in lossy dielectric materials Q_{gen} can be defined as the following [22][23].

$$\langle \boldsymbol{Q_{gen}}\rangle = (\boldsymbol{\sigma} + \boldsymbol{\omega\varepsilon''})\frac{|\mathbf{E_o}|^2}{\mathbf{2}} \tag{1.17}$$

$\boldsymbol{Q_{gen}}$ is the energy deposited by the EM wave into the medium, **σ** is the conductivity of the medium in a static field, **ω** is the angular frequency (rad/s), **ε''** is the complex permittivity, and $\mathbf{E_o}$ (C/m) is the electric field magnitude. Since biological tissue is a lossy dielectric, electromagnetic energy propagating through tissue is absorbed leading to heating.

Objectives

It is desirable to improve focal heating of the tumor to ensure proper treatment, while minimizing damage to surrounding healthy tissue. Due to the limited electromagnetic contrast between healthy and targeted tissue (i.e. tumor cells), there is a large burden on device design to limit electromagnetic radiation in critical structures. In this thesis, I investigated two approaches for increasing focal heating. In the first approach, the design and experimental characterization of a directional interstitial microwave antenna. This was achieved by augmenting a conventional coaxial monopole antenna with a metallic reflector, to limit electromagnetic radiation to a

preferred direction. From Maxwell's equation (eqn 1.4) it can be seen that when an EM microwave has a highly conductive medium in its path, it will result in almost entire reflection of the wave at the boundary. Focal heating for microwave ablation by adding a reflector into current applicator designs is discussed further in Chapter 2.

The second approach is the use of a contrast agent to make the tumor more lossy compared to surrounding tissue. Since, the body does not exhibit magnetic losses the use of magnetic nanoparticles (MNPs) as a contrast can be used to increase energy deposition in a selected region through energy transferred from the **E** and **B**-field. The resulting heat generated by both a dielectric and magnetic lossy material is defined by the Poynting vector for steady state shown in Equation 18 [26].

$$\mathbf{Q_{Gen}} = \mathbf{Re}\{-\boldsymbol{\nabla}\cdot\mathbf{S}\} = (\boldsymbol{\sigma} + \boldsymbol{\omega\varepsilon''})\frac{|\boldsymbol{E_o}|^2}{\mathbf{2}} + \boldsymbol{\omega\mu''}\frac{|\boldsymbol{H_o}|^2}{\mathbf{2}} \tag{1.18}$$

By depositing a magnetically lossy material such as magnetic nanoparticles to a tumor can result in elevated heating compared to just the tissue alone. Chapter 3 investigates the effect of varying nanoparticle shape and geometry on electromagnetic absorption for potential application to microwave tissue heating.

Chapter 2 - A directional interstitial antenna for microwave tissue ablation: theoretical and experimental investigation*

Abstract

Microwave ablation (MWA) is a minimally invasive thermal therapy modality increasingly employed for the treatment of tumors and benign disease. For successful treatment, complete thermal coverage of the tumor and margin of surrounding healthy tissue must be achieved. Currently available interstitial antennas for MWA have cylindrically symmetric radiation patterns. Thus, when treating targets in proximity to critical structures, caution must be taken to prevent unintended thermal damage. A novel coaxial antenna design for MWA with an asymmetrical cylindrical heating pattern is presented in this paper. This radiation pattern is achieved by employing a hemicylindrical reflector, positioned a critical distance from a conventional coaxial monopole antenna. Finite element method simulations were employed to optimize the geometric dimensions of the antenna with the objective of minimizing the antenna reflection coefficient at the 2.45 GHz operating frequency, and maximizing volume of the ablation zone. Prototype antennas were fabricated and experimentally evaluated. Simulations indicated an optimal *S*11 of -32 dB at 2.45 GHz, in close agreement with experimental measurements of -29 dB. Ex vivo experiments were performed to validate simulations and observe effects to the antennas' heating pattern with varying input power and geometry of the reflector. Ablation zones up to 20 mm radially were observed in the forward direction, with minimal heating (less than 4 mm) behind the reflector.

---

* This chapter has been accepted for publication as: B. T. McWilliams, E. E. Schnell, S. Curto, T. M. Fahrbach, and P. Prakash, "A directional interstitial antenna for microwave tissue ablation: theoretical and experimental investigation," IEEE Transactions on Biomedical Engineering, *In Press*, http://dx.doi.org/10.1109/TBME.2015.2413672

Introduction

Microwave ablation (MWA) is an increasingly used thermal therapy for minimally-invasive treatment of tumors and benign disease [27]. Other energy sources for thermal ablation include radiofrequency [8], lasers [9], catheter-based ultrasound applicators [6], and cyroablation [28]. Ablation modalities employing hot sources (e.g., ferromagnetic seeds[29], thermal conductive probes[10], and thermochemical reactions [7]) have also been investigated. These procedures may be performed minimally invasively, typically under guidance of ultrasound or computerized tomography, during open surgery. MWA has found clinical applications in the treatment of tumors in the liver [16], kidney [18], lung [19], and bone [17], as well for treatment of cardiac arrhythmias [14], [15]. During an ablation procedure, an antenna is inserted into the target tissue, and radiates electromagnetic energy at microwave frequencies; most currently available devices operate within frequency bands approved for industrial, scientific, and medical (ISM) use, centered at 433MHz, 915 MHz and 2.45 GHz. Electromagnetic energy radiated from the antenna is deposited in the lossy tissue leading to heating via dielectric hysteresis. While thermal damage following ablation is a complex function of the time-temperature history during heating, temperatures in excess of 60 °C lead to near-instantaneous cell death [2]. A fundamental principal of successful ablation is the creation of an ablation zone that sufficiently covers the entire tumor and margin of healthy tissue to reduce chances of recurrence, while providing a margin of safety for adjacent structures.

In most microwave ablation procedures, the antenna is inserted into the center of the targeted tissue, and the ablation zone grows radially outward. When ablating targets in proximity to critical structures, caution must be taken to ensure complete thermal coverage of the target volume, while precluding thermal damage to non-targeted tissues. Fluid installation between the

target site and organs at risk of injury has emerged as a practical technique for minimizing heating of non-targeted tissues [30]. Availability of an antenna with a directional radiation pattern may simplify the treatment of targets in proximity to critical structures without requiring fluid displacement. Conventional microwave ablation antennas are based on coaxial antenna designs, have axially symmetric radiation patterns, and do not offer control of the energy deposition pattern in the angular expanse [31], [32]. Spatial control of the energy deposition pattern is limited to control of heating along the antenna length, achieved by employing a sleeve/choke [34]. While multiple antennas operated as a phased-array may offer some limited steering of power deposition, the increased invasiveness and system complexity are drawbacks compared to the use of single applicators [33].

Ablation antennas affording spatial control of energy deposition pattern may provide a practical and effective method for heating tumors in proximity to critical structures. Berube and Gauthier [35] designed a directional antenna for ablation of epicardial tissue, employing a reflector-based design, and requiring the use of an impedance matching network to match the antenna to the transmission line. Edwards et al. [36] proposed a design of a directional antenna by placing a microwave absorbent disposed peripherally in one direction, in order to reduce the rear radiation. Debicki et al [37] developed a 25 mm outer diameter (OD) 915 MHz transrectal hyperthermia device for radiating prostate carcinomas. Their design employed a series of conductive tubes to scatter and reflect microwave energy in a direction towards the prostate. While this device was capable of a directional radiation pattern, its large size makes it impractical for percutaneous tumor ablation. Catheter-based ultrasound applicators operating at 6-9 MHz incorporating angular and axial control of the spatial energy deposition pattern have been developed for interstitial and endoluminal ablation of various targets [6], [38], [39].

This study presents a 2.45 GHz microwave antenna with a directional power deposition pattern for tumor ablation. The proposed device may be well suited for targeting tumors and benign disease in proximity to critical structures such as nerves, bowel, bladder, rectum, and the chest wall. Potential clinical sites of interest include peripheral lung tumors, prostate tumors [40], renal tumors in proximity to the ureter or bowel [41], and breast tumors in proximity to the chest wall [42]. The applicator consists of a coaxial antenna with a hemicylindrical reflector to control the deposition of the electromagnetic energy towards the direction of the target, with minimal heating of tissue in the reverse direction. In order to reduce the antenna dimensions, minimize heating of the ablation applicator, and cool the interfacing tissues, the coaxial antenna and reflector were inserted in a 3.5 mm (OD) catheter filled with circulating water. The optimized antenna is well matched to tissue at 2.45 GHz and does not require the use of an impedance matching network. Section II details: numerical simulations employed to optimize the antenna design; antenna fabrication; and experiments performed to evaluate prototype designs in ex vivo tissue. Results from simulations and experimental evaluations are provided in Section III. The performance of this antenna is further analyzed and discussed in Section IV. The paper concludes with a summary in Section V.

Materials and Methods

A simulation-based approach was employed to optimize the design of a directional MWA applicator. The key performance criteria during the design phase were (1) the efficient transfer of energy into the tissue (i.e. minimizing reflected power), and (2) ensuring a directional radiation pattern with minimal heating in the reverse direction. After determining optimal antenna dimensions from simulations, proof-of-concept antennas were fabricated and experimentally

assessed in ex vivo porcine muscle to evaluate: impedance matching, ablation zone pattern, and transient temperature profiles.

Directional Antenna Design

Figure 2.1 shows the schema of the proposed directional antenna in longitudinal and transverse sections. The applicator consists of a coaxial monopole antenna, with a hemicylindrical metallic reflector positioned to ensure propagation of electromagnetic energy in the forward direction. The four geometric parameters a, b, c, and d were varied to minimize the antenna reflection coefficient (S11). Initial simulations suggested a low antenna reflection coefficient could be achieved when the monopole-reflector spacing, d, was approximately 1/10 the wavelength. In order to keep d practically small while maintaining low S11, a material with high dielectric constant (water, $\varepsilon r = 78.6$ at 2.45 GHz) was employed [43]. UT-47 coaxial cable (151-0002, Micro-coax, Philadelphia, PA) was employed to implement the monopole antenna. The UT-47 cable was inserted into a 2.4 mm (OD) stainless steel tubing (McMaster-Carr, Elmhurst, IL), which served as the reflector structure. Using a custom 3D printed bracket, the monopole was set in its optimized location. The stainless steel tube has one end secured with adhesive to a hemostasis valve (Qosina, Edgewood, NY) to create the inflow port for water. The other end of the tube had a section of the metal removed in the desired direction of radiation. A Y-adapter (Qosina, Edgewood, NY) was connected to the hemostasis valve to act as the outflow port for water cooling. A 3.5 mm (OD) polyimide catheter (American Durafilm, Holliston, MA) was placed over the stainless steel tube and connected with adhesive to one end of the Y-adapter. The distal end of the polyimide catheter was sealed with epoxy.

Figure 2.1: Orthographic view of the directional antenna with (a) longitudinal side view along the length of the antenna and orthogonal to opening of directional antenna and (b) transverse view taken through two cross sections.

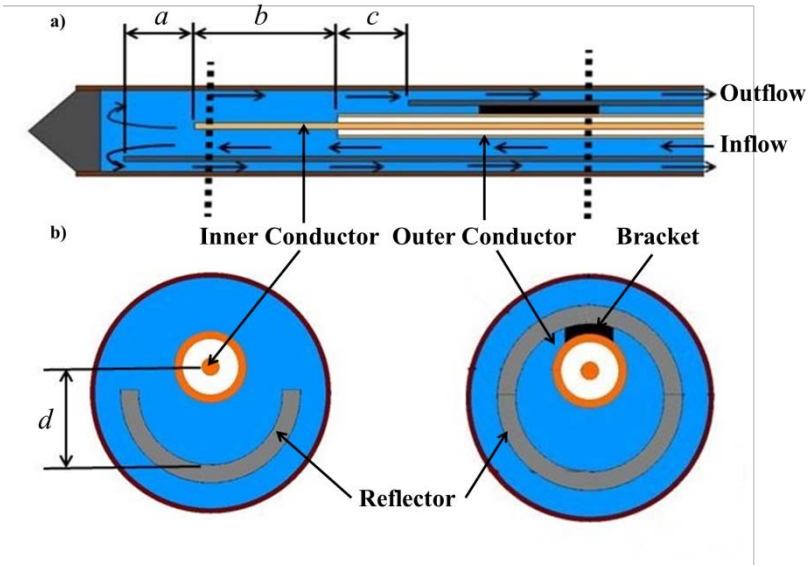

FEM Frequency Domain Model of MWA

A 3D commercial FEM solver (COMSOL Multiphysics v4.4, COMSOL, Inc., Burlington, MA) was used to model electromagnetic energy radiation and subsequent heating from the directional applicator with the geometry shown in Fig. 1. The model was employed to solve the Helmholtz electromagnetic wave equation:

$$\nabla^2 \mathbf{E} - \mathbf{k_0^2}\left(\boldsymbol{\varepsilon_r} - \frac{\mathbf{j\sigma}}{\boldsymbol{\omega\varepsilon_0}}\right)\mathbf{E} = \mathbf{0} \tag{2.1}$$

where, **E** [V/m] is the electric field, k_0 [m^{-1}] is the free-space wavenumber, ε_r is relative permittivity, σ [S/m] is effective electrical conductivity, ω [rads/s] is angular frequency, and ε_0 [F/m] is permittivity of free-space. We modeled a 80 mm long antenna placed at the center of 80 mm diameter cylinder with properties of liver tissue. Table 1 lists the electromagnetic properties of all materials used in our simulations at 2.45 GHz.

Table 2.1: ELECTROMAGNETIC PROPERTIES AT 2.45 [GHZ] USED IN SIMULATION

Material	Permittivity ε_r	Conductivity σ[S/m]
Liver [44]	43	1.69
Water [43]	78.6	1.45
PTFE [24]	2.03	0
Polyimide Tubing [24]	3.4	0

A scattering boundary condition was applied to the outer surface of the simulated liver region to minimize reflection of incident EM waves. All metallic regions were modeled as perfect electric conductors (PEC), implying $\sigma \to \infty$. A coaxial port boundary condition was applied on the surface of the dielectric material of the coaxial line on the top of the cylinder, to specify the desired forward power. A non-uniform mesh of tetrahedral elements was applied, with finest mesh at the antenna feed boundary (maximum edge length 0.005 mm), and relatively coarser mesh in liver tissue furthest away from the antenna (maximum edge length 4 mm). This mesh resolution was determined following iterative adjustments to satisfy a Cauchy convergence test on the S_{11}, (2) [45].

$$|\boldsymbol{S'_{11} - S_{11}}| \leq \mathbf{0.1\ dB} \tag{2.2}$$

where, S'_{11} is the result of a coarser mesh, and S_{11} is the result of the original mesh. The complete mesh consisted of approximately 400,000 elements. Simulations were run on a 12 core Pentium processor with 64 GB RAM operating Red Hat Linux. A single simulation took approximately 40 minutes to complete. Parametric sweeps were used to optimize the antenna dimensions (see Fig. 1) with the objective of minimizing the antenna reflection coefficient at 2.45 GHz. The parameters a, b, and c were varied from 1 mm to 10 mm in 1 mm increments, while parameter d was varied from 2.5 mm to 4 mm in 0.25 mm increments. Following the optimization process, a frequency sweep was performed from 2 to 3 GHz in 100 MHz steps to characterize the frequency response of the antenna. The power deposited by the antenna into the tissue was calculated using (3).

$$Q = \mathbf{J} \cdot \mathbf{E} \tag{2.3}$$

where Q [W/m3] is volumetric power deposition, J [A/m2] is current density, and E [V/m] is electric field intensity. A heat transfer model was employed to solve Pennes' bioheat equation (18).

$$\boldsymbol{\rho c_l \frac{\partial T}{\partial t} = \nabla \cdot (k \nabla T) + Q - \dot{m}_{bl} c_{bl} (T - T_b)} \tag{2.4}$$

Where ρ is density of liver (1050 kg/m3), c_l is the specific heat capacity of liver at constant pressure (3600 J/kg/K), k is the thermal conductivity of liver (0.51 W/m/K), Q [J] is energy deposited into the liver defined by (3), ($\dot{m}_{bl}$) [kg/(m3s)] is blood mass perfusion rate, c_{bl} is the specific heat capacity of blood at constant pressure (3600 J/kg/K), and T_b is the temperature of blood (37 °C). Thermal insulation boundary conditions were applied at the outer extents of the computational domain. To approximate catheter cooling, a fixed temperature boundary condition (20 °C) was applied on the catheter surface [46]. The 52 °C isotherm was used to approximate extents of ablation zone following 10 minute ablations in ex vivo tissue [47]. We considered perfusion values of 0 (ex vivo tissue), 3 (low perfusion tissues such as prostate), and 10 kg/m3/s (high perfusion tissues such as the kidney and liver). For all in vivo simulations, blood perfusion was reduced to 0 kg/m3/s at tissue temperatures in excess of 60 °C to approximate the effects of microvascular stasis. Estimates of the ablation zone for in vivo simulations were determined using an Arrhenius model (1) [4]. For in vivo simulations, the region of ablation was approximated with the Ω=1 threshold after 10 minutes of heating. Fig. 2 illustrates the dimensions of the ablation zone assessed to evaluate the directionality of candidate antenna designs. For nominal antenna designs, the reflector geometry was a half cylinder (θ = 90°). Further simulations were performed varying θ from 10° to 110° in 10° increments. The extents of the ablation zone were characterized by the dimensions r (radial extent of the ablation zone in the forward direction), r' (radial extent of the ablation zone in the reverse direction), and w (width of the ablation zone), as shown in Fig. 2. We considered applied power levels of 50 W and 80 W, 10 min heating durations. Simulations were employed to determine the impact of the reflector enclosure around the antenna on the reflection coefficient and heating pattern.

Figure 2.2: Reflector geometry defined by variable θ. Fiber-optic temperature probes were placed 10 mm in front and 5 mm behind from the center of the antenna at the locations marked x.

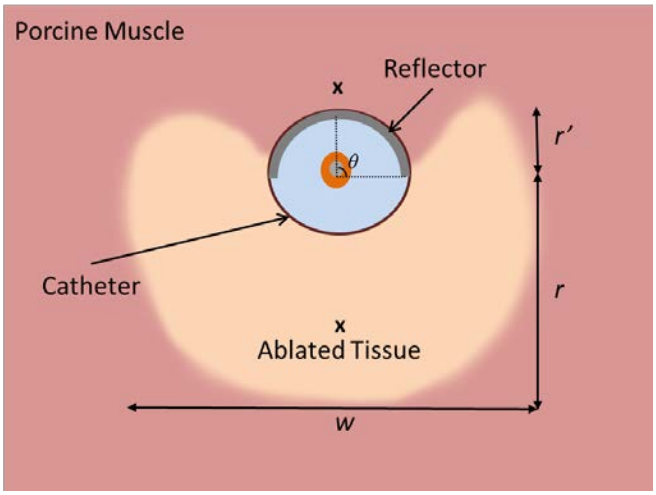

Experimental Evaluation

Proof-of-concept directional antennas were built using the optimized antenna dimensions determined from the procedure described in section II.A. The broadband reflection coefficient for fabricated antennas was measured using an HP 8753D vector network analyzer. Measurements were conducted with room temperature circulating tap water with the antenna inserted to a depth of at least 50 mm in ex vivo porcine muscle. Heating experiments in ex vivo porcine tissue were performed with an input power of 50 W and 80 W using the fabricated antennas to compare to simulation. Porcine muscles, enclosed within water-sealed bags, were heated to ~30 °C in a temperature controlled water bath. Fiber optic temperature probes (Neoptix RFX-04-1, Canada) were placed as shown Fig. 2. Room temperature tap water was circulated through antenna at a flow rate of 5 ml/s with a peristaltic pump (Cole-Parmer, 7554-90, IL). Fig. 3 illustrates the experimental setup for ex vivo ablations in porcine tissue.

Figure 2.3: System for experimental assessment of antennas in ex vivo tissue

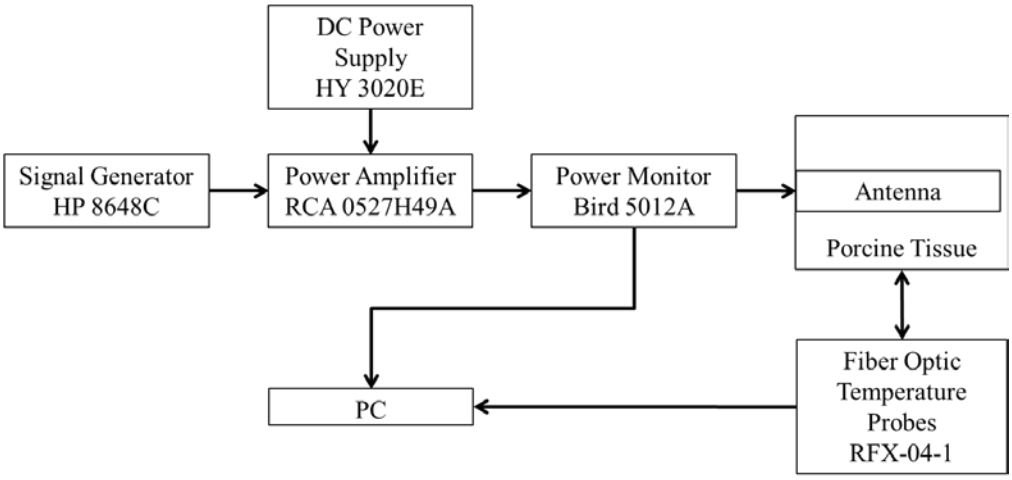

Five experimental ablations were performed for each input power of 50 W and 80 W applied for 10 min. Following ablations, tissue samples were sliced perpendicular to the length of the antenna at the depth that was approximately the position of the tip of the monopole to measure and photograph the area of tissue ablation.

Results

Fig. 4 illustrates simulated and measured reflection coefficient of the optimized antenna design. Simulations determined the optimized values at 2.45 GHz for the antenna dimensions a, b, c, and d, to be 3 mm, 6 mm, 3 mm, and 1.2 mm, respectively. Simulations indicated a minimum S11 of -39 dB at 2.47 GHz with a -15 dB bandwidth of 210 MHz. Measurements with fabricated antennas indicated a minimum S11 of -32.6 dB at 2.49 GHz with a -15 dB bandwidth of 390 MHz. Simulations indicated S11 at 2.45 GHz remained under -20 dB for insertion depths ranging from 3-8 cm.

Figure 2.4: Measured and simulated S11 frequency response of directional Antenna

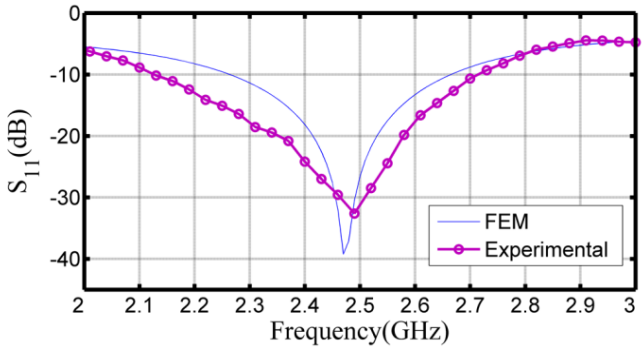

Fig. 5 depicts changes in S11, and extents of the ablation zone for varying reflector geometries (θ).

Figure 2.5: a) Simulated S11 versus θ, b) Simulated r, r', and w versus θ.

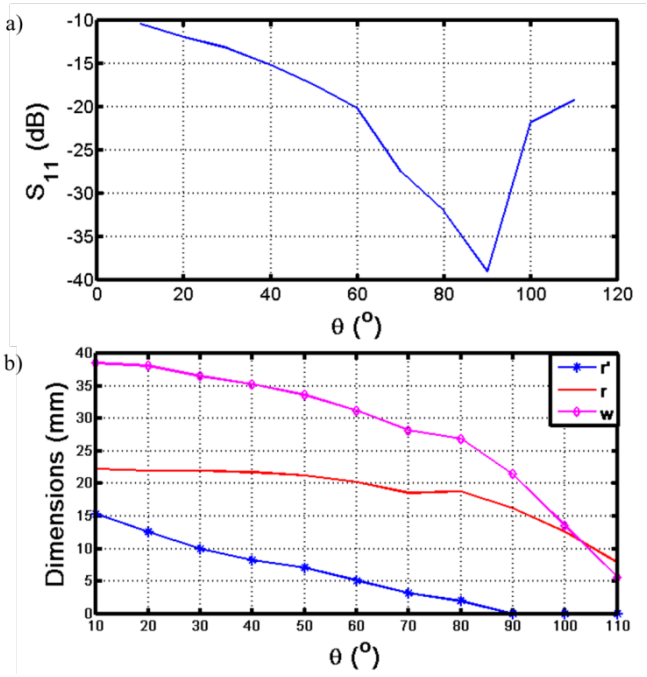

These simulations indicate that θ can be selected to trade off reflection coefficient, width of the ablation zone, depth of forward heating, and extent of backward heating.

Ex vivo heating experiments described in section II.D were performed in porcine tissue using two proof-of-concept antennas, with θ = 90° and θ = 70°, respectively. 90° was chosen as it

was the design with minimal S11 and 70° was chosen since it was the shallowest reflector design (smallest θ) with an S11 below -20 dB. Table 3 lists the dimensions (mean and standard deviation) r, r', and w of the observed ablation zones from slices taken orthogonally for 5 trials.

Table 2.2: EXPERIMENTAL AND SIMULATED AREA OF ABLATION

***θ* [°]**	**90**	**90**	**70**
Input Power [W]	**50**	**80**	**80**
Experimental *r* **[**mm**]**	13.4±1	15.4±0.5	17.6 ±0.5
Simulated *r* **[**mm**]**	13	17.3	21.3
Experimental *r'* **[**mm**]**	1±0.5	2.3±0.5	5.2±2
Simulated *r'* **[**mm**]**	0	.5	5
Experimental *w* **[**mm**]**	22.2±1.3	21.0±0.6	28±0.4
Simulated *w* **[**mm**]**	15.3	23.5	32.5

Experimental values were found to be slightly less than simulated values, with the largest measured difference of 4 mm in w in the trials using a 90° antenna with an input power of 80 W. Fig. 6 shows representative experimental ablation zones as well the thermal simulations for each configuration.

Figure 2.6: Simulated and experimental ablation zones for directional antenna in ex vivo porcine tissue. Temperature patterns in a transverse plane are shown for (a) 90 ° and (c) 70° antenna designs. Also shown are coronal temperature patterns for (b) 90 ° and (d) 70 ° designs. The solid black line represents the 52 ° C boundary and the dashed black, red, and magenta lines represent the boundary of Ω=1 of the Arrhenius integral for blood mass perfusion rates of 0, 3, and 10 kg/m 3/s, respectively. Experimentally observed ablation zones after 80 W heating for 10 min are for 90 ° and 70 ° shown in (e) and (f), respectively

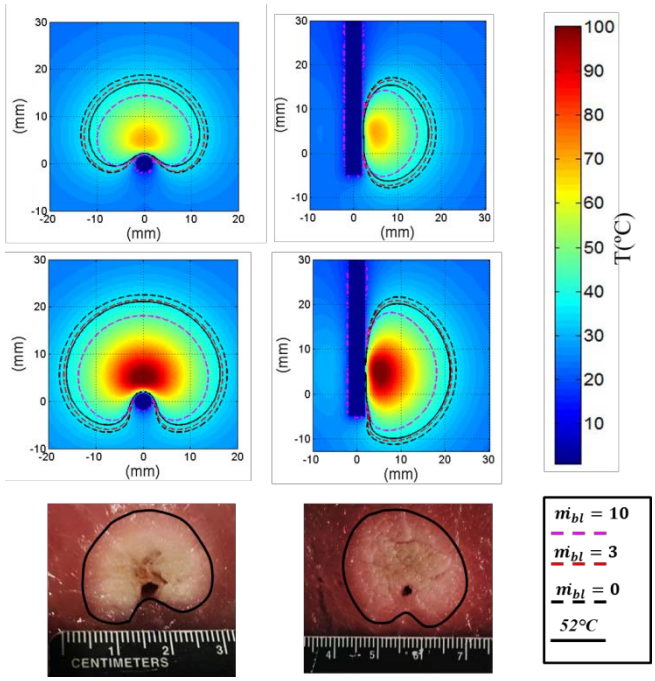

Fig. 7 shows experimentally measured transient temperature profile of four trials in the forward and reverse directions during ablation with a 70° antenna. Input power was set to 80 W for 10 mins. An increase of 61.8±2.5 °C was observed 10 mm radially in the forward direction compared to an increase of 11.1±4 °C 5 mm radially in the reverse direction.

Figure 2.7: Transient temperature profiles (n = 4) measured during experimental ex vivo ablation with a 70° Antenna. A fiber optic temperature probe was placed 10 mm in front and 5 mm behind the antenna to measure the forward and reverse heating, respectively

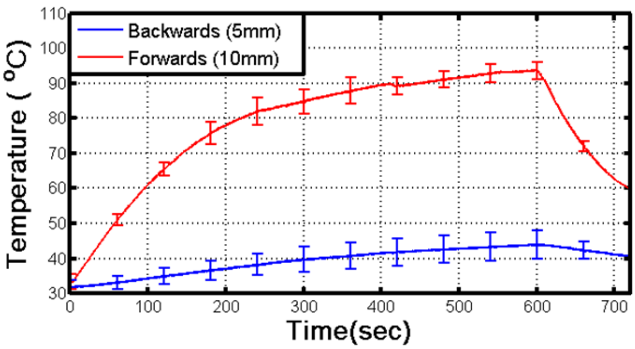

Discussion

This study was undertaken to design a minimally invasive interstitial antenna with a directional radiation pattern for microwave tissue ablation. The proposed antenna design includes a highly conductive reflector to limit radiation in the reverse direction. A simulation-based approached was employed to optimize the antenna dimensions with the goal of minimizing reflected power at 2.45 GHz operating frequency. Proof-of-concept antennas were fabricated and their electromagnetic and heating performance were evaluated in ex vivo tissue.

Initial simulations indicated a relationship between the critical spacing parameter d and the wavelength within the material between the reflector and the monopole antenna. The optimized antenna employed water ($\varepsilon r = 78$ @ 2.45 GHz) as the material between the reflector and the monopole antenna to reduce the critical spacing parameter d, allowing for a constructive interference to occur while also maintaining a relatively small size. Simulations indicated an optimal value of d = 1.2 (mm), yielding an S11 of -32 dB at 2.45 GHz. From 2 to 3 GHz the experimentally measured S11 of the proof of concept antenna exhibited good agreement with simulations (see Fig. 4). Other high dielectric constant materials (e.g., titanium dioxide, $\varepsilon r \sim 100$) may be suitable for further reducing the size of the proposed antenna design. Besides serving as a

high dielectric constant coupling material, circulating water also provides cooling of the catheter shaft, thereby mitigating undesirable heating along the antenna length.

To assess the effect of the reflector geometry on the antenna performance, we evaluated designs with θ varying from 10° to 110°. As shown in Fig. 5a, the antenna reflection coefficient is minimized (S_{11} = -39 dB) when θ = 90°. Good impedance matching (S_{11} < -20 dB, i.e., forward power greater than 99%) is maintained for reflector designs with 60° < θ < 100°. Furthermore, the radial extent of the ablation zone in the forward direction (r) remains fairly constant for θ < 40°. The width (w) and radial extent of the ablation zone in the reverse direction (r') decrease with increasing θ. Simulations indicated that reflectors encompassing a greater extent of the angular expanse (larger θ) yield a more focused heating pattern, with minimal heating in the reverse direction. Decreasing θ led to slight increases in heating in the forward direction, at the expense of greater backward heating. The value of θ had minimal impact on the heating pattern along the length of the antenna. The optimal value of θ can be selected based on the requirements for specific clinical applications, by trading off antenna reflection coefficient, width of ablation zone, and radial extent of the ablation zone in the forward/reverse directions. One potential application is for heating prostate targets with interstitial applicators. Due to the number of sensitive structures in proximity to the prostate (neurovascular bundle, bladder, and rectum), the 90° applicator may be preferable due to the limited backward heating. For endoluminal targeting of prostate structures, further design and optimization of antennas is needed.

The observed shapes of experimental ablation zones were in good agreement with patterns predicted by models. For the 90° antenna, increasing applied power from 50 W to 80 W, yielded on average a 2 mm increase in radial extent of the ablation zone, in good agreement with model predictions (4.25 mm increase predicted by simulations). However, no changes in width

of experimental ablation zones were observed. Both models (4 mm) and experiments (2.2 mm) indicated increases in r for the 70° antenna compared to the 90° antenna. Ablation zones with the 70° antenna exhibited minimal charring of tissue. All experimental ablation zones with the 90° indicated charred tissue in the forward tissue. These observations support the hypothesis that increasing θ leads to more focused heating, while decreasing θ leads to larger ablation zones, at the expense of greater reverse heating. Temperature measurements during ex vivo ablations for a 70° further demonstrated directionality of heating. Peak temperature rise 10 mm in the forward direction on average reached 93.7±2.5 °C, compared to ~11.1±4 °C observed 5 mm in the reverse direction.

While currently available devices for microwave ablation do not offer directional control of heating, catheter-based ultrasound technology has been extensively characterized and affords dynamic control of heating profiles along the applicator length and angular expanse [38], [39], [47]. Results from in vivo simulations directional microwave antenna indicate radial penetration of 16 – 21 mm, similar to ablation zone sizes that can be achieved with catheter-based ultrasound devices. Ultrasound technologies also afford dynamic control of heating along the length of applicators, not currently feasible with the proposed directional microwave antenna. A potential benefit of the directional microwave antenna design is the relatively simpler fabrication process, in comparison to ultrasound technologies that require independent feeding of individual transducers, and degassed circulating water.

Clinicians specializing in cancer therapy seek nonsurgical, minimally invasive techniques which provide eradication of tumor cells with preservation of nondiseased surrounding tissue or sensitive structures such as nerves. Currently this demand is met by percutaneous ablation with microwave antennas via image guidance such as computed tomography or ultrasound. The

technical considerations of subjecting a tumor to cytotoxic temperatures may prove difficult, as navigation of a device to within or just beyond the tumor is not always anatomically possible. Operator control of the ablation zone by directional targeting of tumor has the potential to improve the clinical outcomes, safety, efficiency, and cost of tumor ablation treatment. Current ablation devices require a direct approach for intratumoral placement of the antenna. With directional ablation capability, clinicians could alter the angle of approach to lesions that are situated adjacent to critical structures (see Figure 8). Even a slightly different trajectory could be crucial in avoiding intrinsic damage to liver, lung, and other organs, as well as avoiding thermal damage to adjacent structures such as bowel, blood vessels, or nerves. More so, directional technology could potentially allow an alternate, safe percutaneous window for treatment of lesions that were previously inaccessible. Electromagnetic and camera-based needle-tracking and guidance technology may be suitable for estimating applicator coordinates (x,y,z) and orientation (roll, pitch, and yaw) with ultrasound and CT guidance [48], [49], [50]. Another potential solution is to augment the device with fiducial paint, visible on CT, to indicate device orientation.

Figure 2.8: Right adrenal tumor MWA typically necessitates a transhepatic approach (a) which carries risk of damage to the liver, with the solid black line representing the orientation of conventional MWA applicator. A 90 ° microwave antenna would provide provide (b) an alternate trajectory that avoids the liver, kidney, and spine, with the arrow showing direction of heating

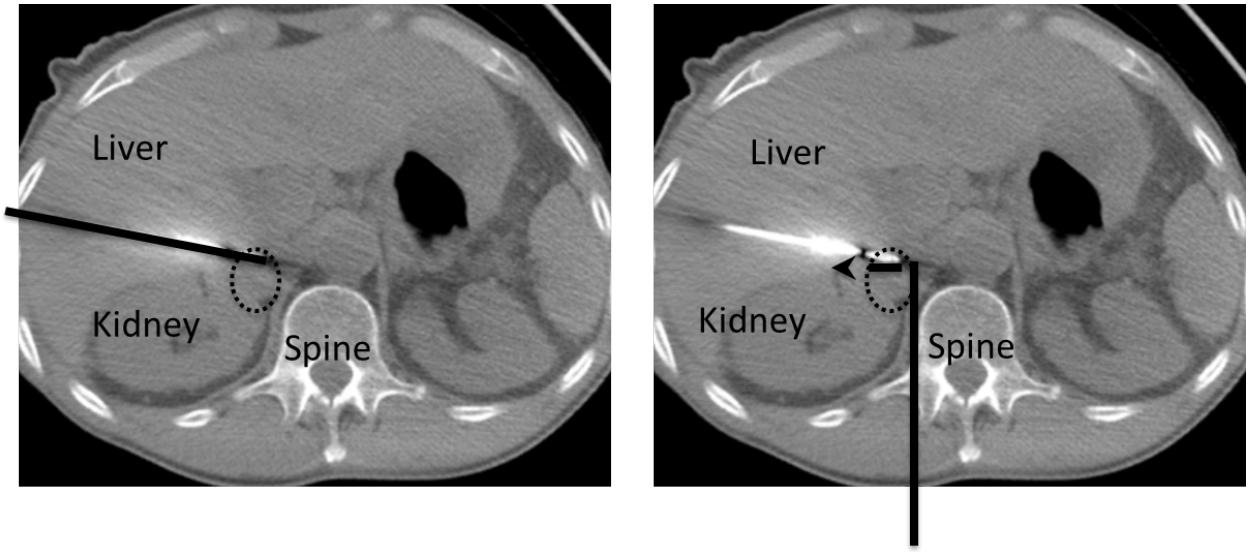

A limitation of the applicator design presented in this study is the relatively large diameter (O.D. = 3.5 mm). Reduction of the applicator diameter may be achieved by using smaller coaxial cables, implementing the reflector directly on a catheter inner-wall, and exploring the use of low-loss, high dielectric constant ceramics (e.g. titanium dioxide). With further design optimization, it is possible that directional antennas may find the right niche as an adjunctive or alternate tool for difficult tumor locations. In current form, the relatively small ablation zone diameter places restrictions on targets that may be treated with the proposed technology. Future studies will investigate elevated power levels, and the use of low-loss materials within the catheter to increase power deposition within tissue.

Conclusion

In this paper, we utilized a simulation-based approach to design and optimize an interstitial MWA antenna with a directional radiation pattern. Proof-of-concept antennas were

fabricated and experiments were conducted to evaluate their reflection coefficient and heating performance in ex vivo porcine tissue. Simulations and experimental data showed good agreement for the broadband antenna reflection coefficient and the antenna heating pattern. Experimentally measured transient temperature profiles indicated significantly more rapid heating to larger temperatures in the forward direction, with temperature rise in the reverse direction limited to 15 °C. Furthermore, measurements of the volume of ablation showed that varying the enclosure and input power only marginally increased the penetration depth characterized by the parameter r. Further studies will need to be performed to further characterize the effects of the reflectors' geometry on the radiation pattern, and to reduce the effects associated to the water cooling of the antenna. The modeling and optimization techniques presented in this paper can be extended to designs of interstitial MWA directional antennas for different target organs.

Chapter 3 - Nanoparticle-enhanced microwave hyperthermia: effects of nanoparticle size and shape on heating

Abstract

Purpose: Effective hyperthermia treatments require the delivery of sufficient therapeutic heating to the target volume, while minimizing thermal damage to non-targets. Limited electromagnetic contrast between malignant and healthy cells places a large burden on the design of devices and strategies to focus energy within the target volume. To ease this burden, nanoparticles with dielectric and/or magnetic contrast have been proposed to increase the coupling of the electric and/or magnetic field during microwave heating. Magnetic nanoparticles (MNPs) offer the potential to enhance microwave hyperthermia by increasing the electromagnetic contrast between tumor and healthy tissue.

Materials and Methods: An experimental testbed consisting of a glass capillary tube (1.33 mm) I.D, filled with MNPS placed in solution of 2% agarose and placed in WR340 waveguide. Microwave radiation (2.0-2.6 GHz, 15 W, 3 min) was injected into one waveguide port, with the other port terminated with a matched load. A fiber-optic temperature probe inserted into the capillary tube monitored temperature of MNP solutions during and after heating. The following MNPs, coated with 0.05% dopamine, were evaluated: 10 and 20 nm diameter spherical Fe/Fe_3O_4, 20 nm edge-length cubic Fe_3O_4, and 45 nm edge-length/10 nm height hexagonal Fe_3O_4. MNP heating enhancements were experimentally (n=5) evaluated at concentrations of 1 g/50ml, 1 g/100ml and 1 g/200ml. A 0.05 % solution of dopamine in deionized water was used as a control. Further tests with 20nm spherical MNPs distributed uniformly in a 20 mm radius sphere of agar were performed with a conventional dipole operating at 2.45 GHz and radiating

15 W. temperature probes were placed 5 mm, 10 mm, and 15 mm radially away from the dipole and 3 heating experiments were performed.

Results: For the waveguide measurements, the control group exhibited an average temperature rise of 25.4 ± 0.5 °C. At a concentration of 10 mg/ml, solutions of 10 nm spherical, 20 nm spherical, hexagonal, and cubic MNPs yielded an average temperature increase of 49.4 ± 1.2 °C, 44.6 ± 0.7 °C, 30.2 ± 0.7 °C, and 24.2 ± 0.5 °C, respectively. At reduced concentrations of 5 mg/ml, 10 nm, 20 nm spherical and hexagonal MNPs yielded temperature increases of 38.1 ± 0.6 °C, 35.5 ± 0.9 °C and 25.8 ±0.6 °C, respectively. With the distributed volume of 20 nm MNPs an initial heating rate taken 10 mm from the radiating source exhibited an increase of 4 times that of the control group.

Conclusions: The MNPs considered in this study offer strong potential to offer heating enhancements during microwave thermal therapy procedures. Ongoing efforts are investigating the broadband complex dielectric and magnetic properties of the candidate nanoparticles in solution. Future research investigating nanoparticle delivery techniques and *in vivo* evaluation of heating is warranted.

Introduction

Hyperthermia is a thermal therapy, where a region of the body is heated in the temperature range of 39 °C - 43 °C with an external energy source. Hyperthermia has been shown to improve treatment of cancer adjunctive with chemotherapy or radiotherapy [51], [52], [53]. Hyperthermia therapies can be categorized as local, interstitial, regional, and whole-body hyperthermia, depending on the volume of heated tissue during treatment [54]. Whole-body hyperthermia is a procedure which raises the patient body temperature to 41°C for a certain duration of time and offers no focal heating [55]. Local hyperthermia is limited by its penetration

depth and will not be able to adequately heat deep seated tumors e.g. located in the pelvis or abdomen [55]. Interstitial and regional heating can be used for deep seated tumors at the expense of a more invasive or complex procedure respectively. Furthermore, different modes of power deposition have been investigated for hyperthermia *i.e* resistive, capacitive, inductive, convective, and radiation [56], [57].

Various FDA approved non- and minimally invasive devices employing radio frequency and microwave modalities are discussed in detail elsewhere [58],[59],[60]. Current microwave, interstitial and non-invasive, devices have been approved for 915 MHz and 2.45 GHz. Some current hyperthermia devices include the BSD-500 and BSD-2000 annular phased array [57],[61]. A significant challenge associated with hyperthermia treatment is the focused delivery of energy to minimize damage to healthy tissue, while sufficiently treating the cancerous tissue target. Improved focusing can be achieved by either designing applicators with focal radiation patterns, or the physical properties of the targeted tissue to increase the contrast between tumor and healthy tissue. Chapter 2 covers modification of a catheter based microwave applicator for directional heating. The contrast of the dielectric properties of malignant tissue compared to healthy is approximately 19 to 30% for the 0.5-20 GHz frequency range and 6% for the 50-900 MHz frequency range[62], [63], and [64]. Various nanoparticle contrast agents have been investigated as a method of increasing heating of malignant tissue compared to healthy tissue [65], [26].

MNPs have been studied as a contrast agent for AC hyperthermia and are FDA approved for clinical use. They have been shown to be biocompatible and are able to be passively or actively guided into the tumors. However, high concentrations are necessary for proper therapy and uncontrollable hot spots form limiting treatment abilities [23]. The use of MNPs in

interstitial microwave hyperthermia could result in contrast heating while avoiding some drawbacks associated to MNP heating. Furthermore, the characterization of microwave heating of MNPs has not been explored in great detail [66]. In this study we explore the heating enhancement of different structured MNPs in the presence of microwave radiation.

Materials and Methods

Fabrication of MNP

10 and 20 nm spherical Fe/Fe_3O_4, 20 nm edge-length cubic Fe_3O_4, and 45 nm edge-length/10 nm height hexagonal Fe_3O_4 were fabricated with a thermal decomposition technique by our collaborators in the KSU Chemistry Department (Dr Stefan Bossmann and Dr. Hongwang Wang). A dopamine coating, to improve solubility, on the molecules contributed to about 5% by weight of the MNP molecular structure. TEM images were performed to ensure the size and structure of the MNPs and are shown in Figures 3.1.

Figure 3.1: TEM imaging of different size and structured MNPs with a) and b) showing 10 and 20 nm spherical Fe/Fe_3O_4 respectively, c) hexagonal Fe_3O_4, and d) cubic Fe_3O_4

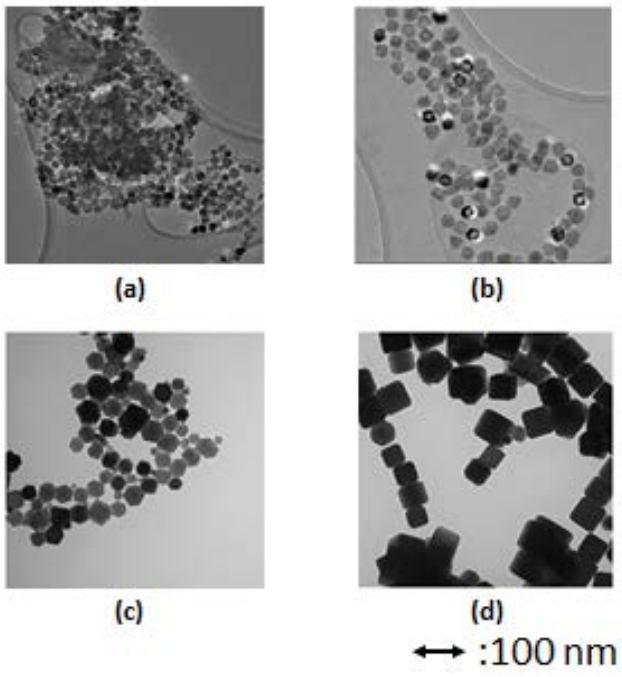

Microwave Measurements

Using the test setup described in [67] the enhancement of heating due to the MNPs interaction with microwave radiation of the respective structures were compared. A 2% water-based agarose phantom was prepared and the respective MNPs were put into solution at concentrations, by weight, of 2%, 1%, .5%, and .025%. Sonication of a solution was performed to ensure uniform dispersion of the respective MNPs in the gel before injection into a capillary tube with a 1.33 mm inner diameter. A fiber-optic temperature probe (Neoptix RFX-04-1, Canada) was inserted into the capillary tube and the gel was allowed to set around the probe. The capillary tube was then placed in a test setup shown in figure 3.2.

Figure 3.2: Test set up used in measuring temperature trends of MNPs

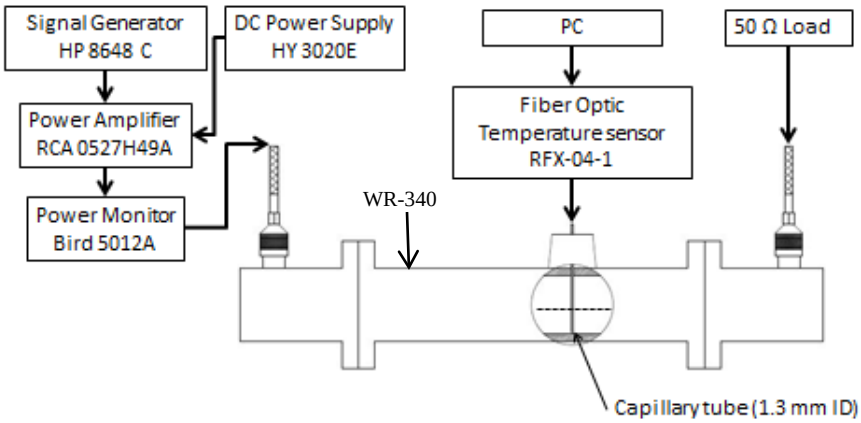

A WR340 (86.36 mm x 43.18 mm x 254 mm) waveguide was used and tuned such that an S_{11} of at least -20 dB in the frequency range of 2.0-2.6 GHz was observed. A hole was drilled into the broad side of the waveguide for placement of the capillary tube. The S_{11} and S_{21} of the waveguide showed no distinguishable change in magnitude due to the hole. To ensure a single pass of the EM wave occurred one of the waveguide ports was connected to a 50Ω load. With the other port radiating a 15 watt EM wave at the frequencies of 2.0, 2.45, and 2.6 GHz. An

agarose gel with .1% dopamine solution was used as a control to compare heating contrasts of MNP and 5 trials at each respective frequency was performed. At 2.45 GHz each structured MNP was put into a 2% concentration and 5 trials were performed, if a heating difference between the control and experimental was observed the solution was diluted to half the concentration, this was done until no heating enhancement compare to control was observed. For trials performed at 2.0 or 2.6 GHz the concentration of the MNP solution was fixed at 1% and 5 trials were performed at each frequency. Between each trial the capillary tube was discarded and replaced in the test set up. Temperature trends were processed in matlab to calculate the slope of the temperature using ten seconds of data immediately after turn off of the signal generator [68]. Since the material does not go through an irreversible change during heating and is at steady state right before turn off, the slope of the temperature with respect to 10 seconds of time was used to estimate the solutions heating rate. The heating rate of a material is proportional to the specific absorption rate (SAR) with a single point temperature as shown (Eqn.3.1).

$$\boldsymbol{SAR = \rho c \frac{\partial T}{\partial t}} \qquad \textbf{(3.1)}$$

Although, this test method is able to compare the MNPs heating properties relative to each other the heating rate of such a small volume does not accurately described what would be observed during hyperthermia treatments in which the MNPs would be distributed throughout a larger volume. Figure 3.3 shows a test setup designed to simulate a more realistic distribution of the MNPs during treatment, a 20mm radius sphere. The concentration of the MNPs distributed in the volume was fixed at 1% by weight.

Figure 3.3: Test set up used in measuring temperature trends of MNPs

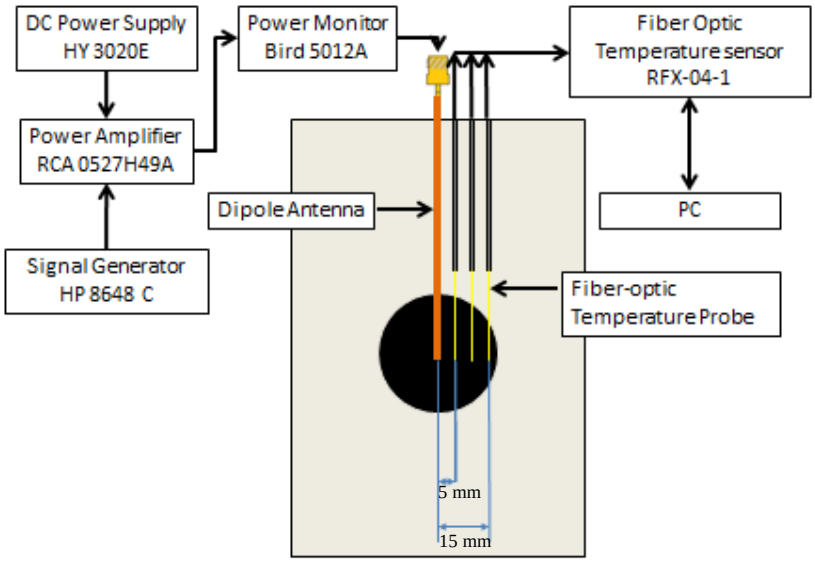

A dipole antenna designed with an operating frequency of 2.45 GHz radiated 15 watts of power from the center of the spherical distributed MNPs. Temperature was measured, using fiber-optic probes, radially 5mm, 10mm, and 15mm from the dipole antenna. 3 trials with a distributed volume of 20 nm spherical Fe/Fe_3O_4 was compared to 3 trials of heating observed with just the agar gel.

Results

Figure 3.2 illustrates the heating due to microwave radiation of the MNPs at different concentrations with 10 and 20 nm spherical, hexagonal, and cubic structures shown in (a), (b), (c), and (d) respectively.

Figure 3.4: Microwave heating temperature trends of MNPs agar with respect to concentration and molecular structure of MNP. (n=5) for all variations

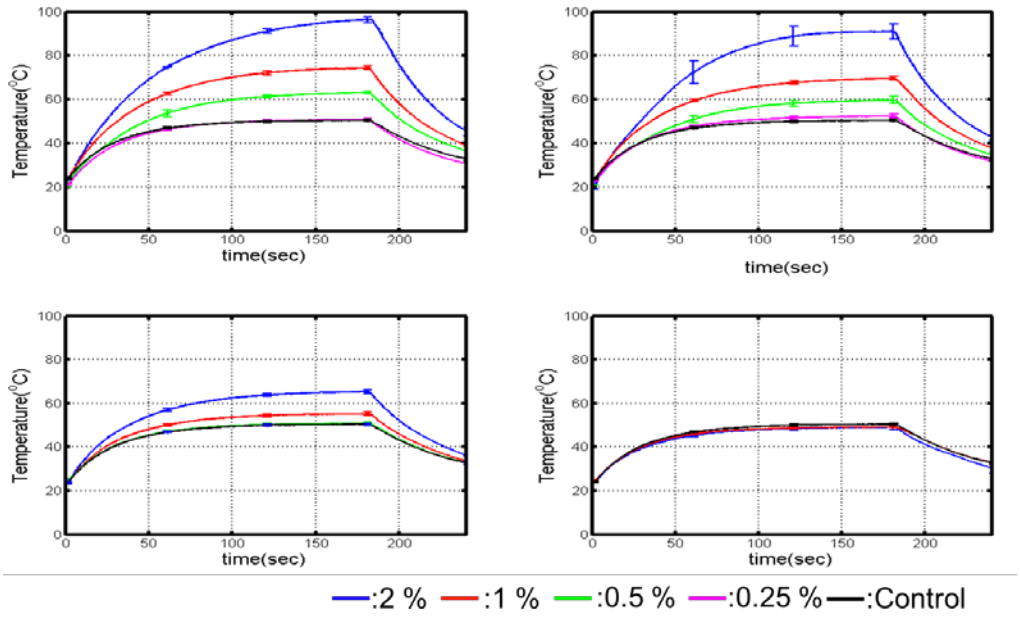

Experimental data shows higher temperature rise compare to control for higher concentrations of 10 and 20nm spherical and hexagonal MNP solutions. A maximum temperature of 50.4 ± 0.5 °C was observed for the control group at 2.45 GHz. Cubic MNPs showed no distinguishable heating difference from the control group with cubic showing a maximum temperature of 49.0 ± 1°C and 49.2 ± 0.5 with a 2% and 1% concentration respectively. 10nm spherical MNPs showed a maximum temperature of 96.4 ± 1.3 °C, 74.4 ± 0.9, 63.1 ± 0.6 °C, and 50.7 ± 0.6 °C with a 2%, 1%, 0.5%, and 0.25% concentration respectively. 20nm spherical MNPs showed a maximum temperature of 90.9 ± 3.4 °C, 69.6 ± 0.7, 60.5 ± 0.9 °C, and 52.4 ± 0.9 °C with a 2%, 1%, 0.5%, and 0.25% concentration respectively. Hexagonal MNPs showed a maximum temperature of 65.3 ± 0.8 °C, 55.2 ± 0.7 °C, and 50.8 ± 0.6 °C with a 2%, 1%, and 0.5% concentration respectively. Figure 3.4 illustrates the average and standard deviation calculated from theslopes

of each individual temperature trends ofeach respective concentrations and structures shown in figure 3.3.

Figure 3.5: SAR of MNPs agar with respect to concentration and molecular structure of MNP. (n=5)

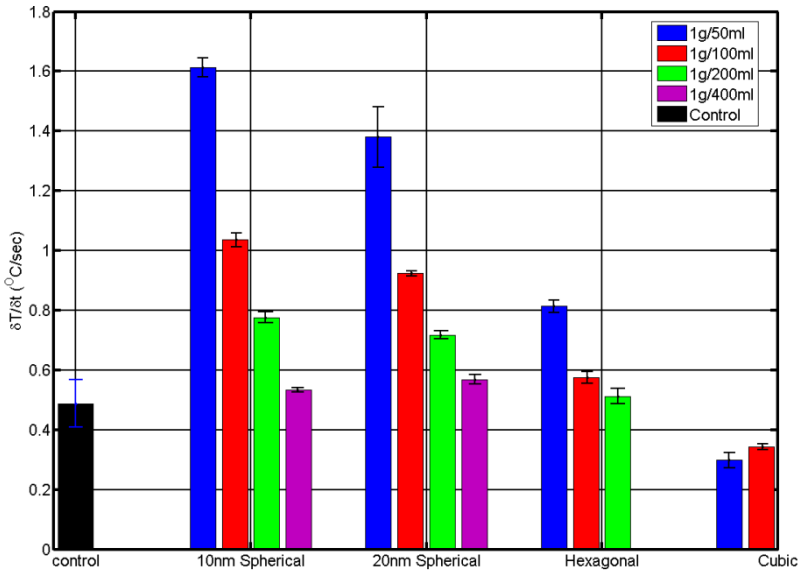

The control trials showed an average slope of 0.5 ± 0.1 °C/s. Cubic MNP solutions showed a slope of 0.3 ± 0.03 °C/sand 0.3 ± 0.01 °C/s with a concentration of 2% and 1% respectively. 10nm MNP solution spherical showed an average slope of 1.61 ± 0.03°C/s, 1.04 ± 0.02 °C/s, 0.776 ± 0.02 °C/s, and 0.53 ± 0.01 °C/s with a concentration of 2%, 1%, 0.5%, and 0.25% respectively. 20nm spherical MNP solutions showed an average slope of 1.38 ± 0.1 °C/s, 0.92 ± 0.01 °C/s, 0.72 ± 0.01 °C/s, and 0.56 ± 0.016 °C/s with a concentration of 2%, 1%, 0.5%, and 0.25% respectively. Hexagonal MNP solutions showed an average slope of 0.81 ± 0.02 °C/s, 0.58 ± 0.02 °C/s, and 0.51 ± 0.03 °C/s with a concentration of 2%, 1%, and 0.5% respectively. Figure 3.5 illustrates the heating of respective MNP solutions with a fixed concentration of 1% at 2.0 GHz, 2.45 GHz, and 2.6 GHz.

Figure 3.6: Microwave heating temperature trends of MNPs agar with respect to frequency and molecular structure of MNP. (n=5)

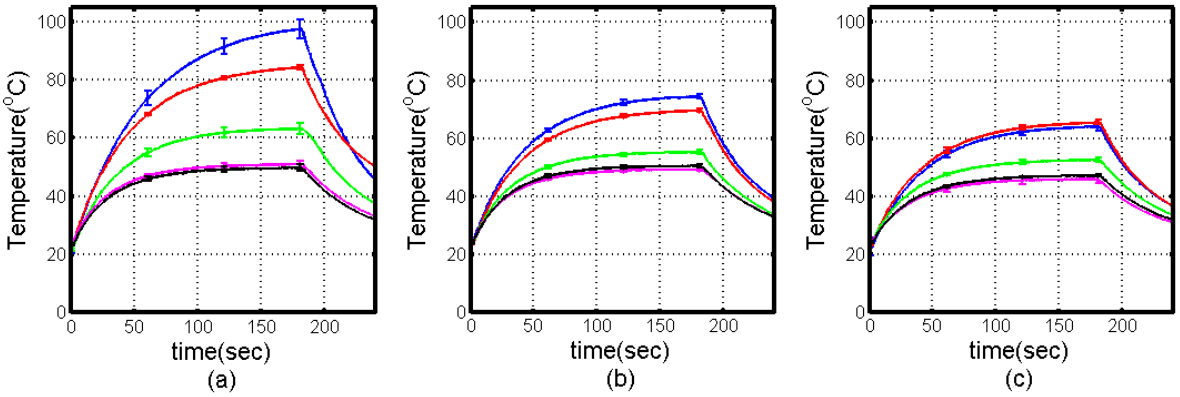

Control trials showed an average maximum temperature rise of 49.7 ± 1.1 °C, 50.4 ± 0.5 °C, and 47 ± 0.3 °C at 2 GHz, 2.45 GHz, and 2.6 GHz respectively. 10nm spherical MNP solutions showed an average maximum temperature rise of 97.6 ± 3.1 °C, 74.4 ± 0.9 °C, and 63.9 ± 1.4 °C at 2 GHz, 2.45 GHz, and 2.6 GHz respectively. 20nm spherical MNP solutions showed an average maximum temperature rise of 84.4 ± 0.8 °C, 69.6 ± 0.7 °C, and 65.5 ± 0.8°C at 2 GHz, 2.45 GHz, and 2.6 GHz respectively. Hexagonal MNP solutions showed an average maximum temperature rise of 63.2 ± 1.9 °C, 55.2 ± 0.7 °C, and 52.4 ± 0.9 °C at 2 GHz, 2.45 GHz, and 2.6 GHz respectively. Cubic MNP solutions showed an average maximum temperature rise of 51.1 ± 1.2 °C, 49.2 ± 0.5 °C, and 45.5 ± 1.2 °C at 2 GHz, 2.45 GHz, and 2.6 GHz respectively. Figure 3.6 illustrates the average and standard deviation of the slopes of each individual temperature trends at the respective frequencies and structures at a 1% concentration shown in figure 3.3.

Figure 3.7: SAR of MNPs agar with respect to frequency and molecular structure of MNP. (n=5)

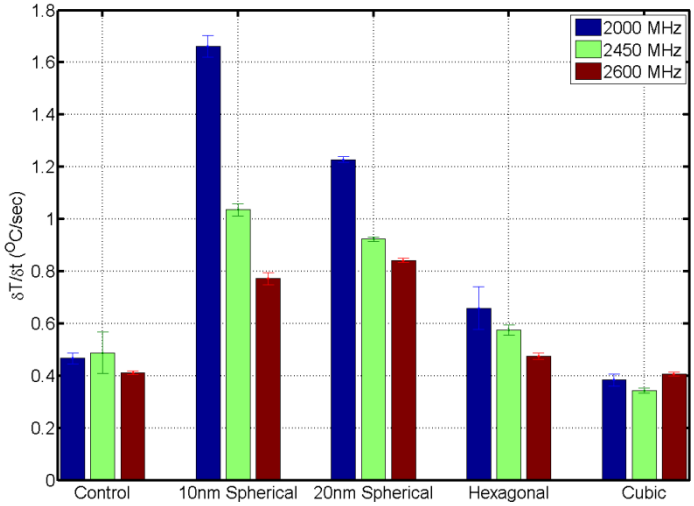

The control trials showed an average slope of 0.47 ± 0.02 °C/s, 0.49 ± 0.08 °C/s, and 0.41 ± 0.01 °C/s at 2.0 GHz, 2.45 GHz, and 2.6GHz respectively. Cubic MNP solutions showed a slope of 0.38 ± 0.02 °C/s and 0.4± 0.01 °C/s at 2.0 GHz, 2.45 GHz, and 2.6GHz respectively. 10nm MNP solution spherical showed an average slope of 1.7 ± 0.04 °C/s, 1.04 ± 0.02 °C/s, and 0.77 ± 0.02 °C/s at 2.0 GHz, 2.45 GHz, and 2.6GHz respectively. 20nm spherical MNP solutions showed an average slope of 1.23 ± 0.01 °C/s, 0.92 ± 0.01 °C/s, and 0.84 ± 0.01 °C/s, at 2.0 GHz, 2.45 GHz, and 2.6GHz respectively. Hexagonal MNP solutions showed an average slope of 0.81 ± 0.08 °C/s, 0.58 ± 0.02 °C/s, and 0.48 ± 0.01 °C/s at 2.0 GHz, 2.45 GHz, and 2.6GHz respectively. Figure 3.7 shows the measured temperature rise of probes placed 5 mm, 10 mm, and 15 mm away from a dipole antenna radiating 15 watts of power at 2.45 GHz as shown in figure 3.2.

Figure 3.8: Microwave heating temperature trends of MNPs agar in a distributed volume (n=3)

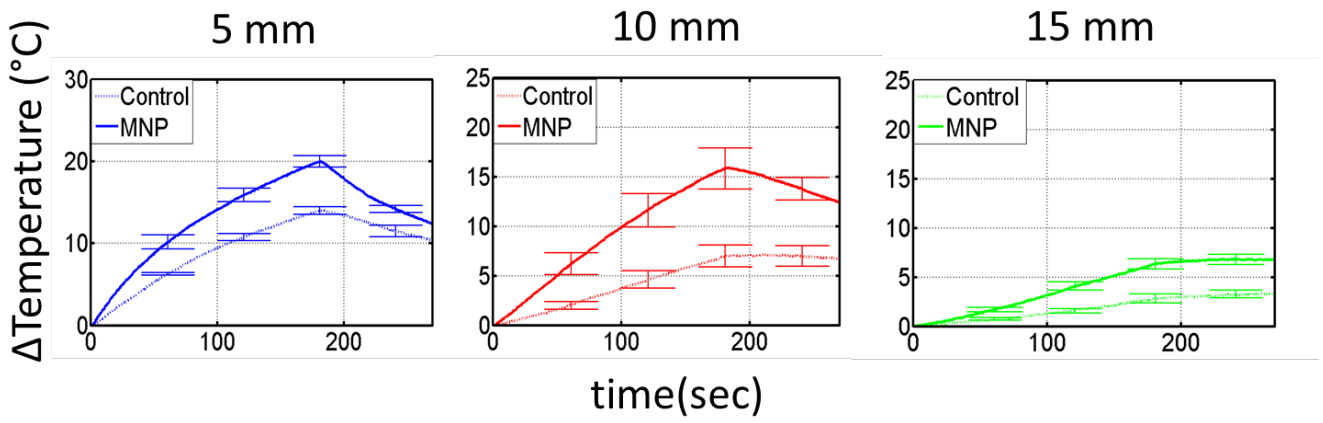

At 5 mm away from the dipole antenna a temperature enhancement of 3.5 ± 0.8 ºC was observed between the MNP and control agar samples. At 10 mm away from the dipole antenna a measured temperature enhancement of 8.8 ± 2.3 ºC was observed between the MNP and control agar samples. At 15 mm away from the dipole antenna a temperature enhancement of 6.0 ± 0.5 ºC was observed between the MNP and control agar samples. With distributed MNPS an average initial heating slope of 0.19 °C/s, 0.08 °C/s, and 0.02 °C/s was observed at 5 mm, 10 mm, and 15 mm respectively. With agar alone an average initial heating slope of 0.09 °C/s, 0.02 °C/s, and 0.003 °C/s was observed at 5 mm, 10 mm, and 15 mm respectively.

Discussion

In this study, 10 nm and 20 nm diameter Fe/Fe_3O_4 spherical MNPs, and 45 nm edge-length/10 nm height hexagonal MNP in 2% agarose solution showed an observable difference in heating compared to the control group in the frequency range of 2.0-2.6 GHz. At 2.0 GHz, 2.45 GHz, and 2.6 GHz, cubic MNP solution did not show any observable increase in heating compared to control. Both spherical and hexagonal structured MNPs solutions showed a higher maximum temperature and a steeper rate of heating was associated with higher MNP

concentrations. Overall, spherical structured MNPs were observed to have a higher maximum temperature and steeper rate of heating compared to hexagonal structured MNPs at similar concentrations.

At 2.45 GHz, 10 nm spherical MNPs showed a higher temperature rise compared to 20 nm spherical MNPs except for the 0.25% concentration, where 20 nm but not 10 nm was still distinguishable from the control trials by approximately 2 °C. Both spherical and hexagonal structured MNP solutions exhibited less heating and lower slopes at higher frequencies in the frequency range of 2.0-2.6GHz. Furthermore, 10 nm spherical Fe/Fe_3O_4 showed an increase of 20°C and 0.63°C/sfor maximum temperature and slope between trials performed in the waveguide at 2.0 GHz compared to 2.45 GHz. 20 nm spherical Fe/Fe_3O_4 did not exhibit a significant difference with an increase of 15 °C and 0.3 °C/s.

Results of the experiments with a dipole antenna showed a temperatuer difference of 3.5 ± 0.8 ºC, 8.8 ± 2.3 ºC, and 6.0 ± 0.5 ºC for 5 mm, 10 mm, and 15 mm respectively. This further indicates the absorption of the EM energy due to the MNPs directly affects the temperature near the antenna as can be seen in figure 3.8 at the peak temperature before turn off, but that the heating increases at greater distances seem to be due to conduction. The change in heating rate between the control and experimental at the distances 10 mm and 15 mm indicates that the thermal conductivity of the MNPs may result to more distributed spread in heating and allow deeper penetration. Therefore, the MNPs may be used as contrast agent thermally and electrically[69]. MNPs could be integrated into interstitial hyperthermia treatments employing microwave energy. Due to the minimally invasive nature of interstitial microwave hyperthermia the insertion needle could inject MNPs into the tumor prior to treatment while still maintaining a minimally invasive procedure. Further work must be performed to understand the thermal and

electric magnetic properties of the MNPs to determine what mechanism is related to heating. MR imaging of heating experiments should be performed as well to better characterize the heating profile of the MNPs in a distributed volume.

Conclusion

MNPs with spherical Fe/Fe_3O_4, hexagonal Fe_3O_4, and cubic Fe_3O_4 composition were compared on microwave heating at various concentrations and frequencies. Considering similar concentrations, spherical structured MNPs showed more thermal enhancement than hexagonal MNP. Cubic showed no heating difference compared to control. Furthermore, it was shown that heating enhancement was greater at 2.0 GHz compared to 2.45 GHz and 2.6 GHz for 1 % concentration of MNP solutions. It was also shown that MNP could potentially improve interstitial hyperthermia procedures with the MNPs distributed into the tumor before thermal treatment. Further studies will need to be performed to better characterize the thermal heating, electric, and magnetic properties of MNPs with respect to broadband frequencies.

Chapter 4 - Conclusion and Future Work

It is desirable to improve focal heating of the tumor to ensure effective thermal therapy treatment, while minimizing damage to surrounding healthy tissue. In this thesis, I investigated two approaches for increasing focal heating was investigated. Chapter 2 covered the design and experimental characterization of a directional interstitial microwave antenna. Chapter 3 covered the evaluation of different size and structured MNPs for thermal enhancement in microwave hyperthermia and ablation.

The study with the directional antenna showed promising results of achieving heating profiles preferential to one direction using the proposed applicator. The current design faces some limitations that must be addressed before clinical application is possible. Reduction in the applicator diameter (current O.D. ~3mm) would increase its suitability for percutaneous ablation. As stated in Chapter 1 of this paper conventional interstitial microwave antennas have an OD <3mm size usually on the order of 1 mm to 2 mm. Reduction of the directional applicator could be achieved by placing the conductive material onto the inner or outer wall of the catheter and offsetting the antenna to one side of the catheter. Furthermore, a large amount of energy is believed to be absorbed by the circulating water and therefore reduces the penetration into tissue. Future work, should be done to characterize the loss of energy in the circulating water, investigating high dielectric and ceramics such as TiO_2 to replace the water, and evaluate the effect of the geometry of the reflector and the observed heating pattern. Furthermore, a more flexible applicator would be desirable as well to allow the applicator to be used intravenously along with optimizing the design for various treatment regions of the body.

MNPs were investigated as possible contrast agents for the enhancement of heating contrast between healthy tissue and tumor in chapter 3. It was determined that MNPs at

concentration in the order of 0.5-2% concentration showed a significant increase in heating compare to control. Although, there is strong evidence supporting possible improvements to interstitial hyperthermia by employing MNPs, the mechanisms behind the observed heating are not understood currently. Future studies should focus on relating physical properties (electrical, magnetic, and thermal) of the MNPs to the enhancement of heating to further optimize the structure and size of the MNPs. Furthermore, possible use of MNPs for thermally-enhanced drug delivery to tumors and the use of MNPs as a contrast agent in MRI should be explored as well.

References

[1] P. Wust, B. Hildebrandt, G. Sreenivasa, B. Rau, J. Gellermann, H. Riess, R. Felix, and P. Schlag, "Hyperthermia in combined treatment of cancer," *Lancet Oncol.*, vol. 3, no. 8, pp. 487–497, Aug. 2002.

[2] W. C. Dewey, "Arrhenius relationships from the molecule and cell to the clinic," *Int. J. Hyperthermia*, vol. 10, no. 4, pp. 457–483, Jan. 1994.

[3] J. J. Cipolloni, F. J. Looft, and S. Virani, "Equipped-human Reference Architecture," *Procedia Comput. Sci.*, vol. 44, pp. 42–51, 2015.

[4] J. A. Pearce, "Models for thermal damage in tissues: processes and applications," *Crit. Rev. Biomed. Eng.*, vol. 38, no. 1, pp. 1–20, 2010.

[5] V. A. Salgaonkar, P. Prakash, V. Rieke, E. Ozhinsky, J. Plata, J. Kurhanewicz, I.-C. (Joe) Hsu, and C. J. Diederich, "Model-based feasibility assessment and evaluation of prostate hyperthermia with a commercial MR-guided endorectal HIFU ablation array," *Med. Phys.*, vol. 41, no. 3, p. 033301, Mar. 2014.

[6] C. J. Diederich, W. H. Nau, and P. R. Stauffer, "Ultrasound applicators for interstitial thermal coagulation," *IEEE Trans. Ultrason. Ferroelectr. Freq. Control*, vol. 46, no. 5, pp. 1218–1228, Sep. 1999.

[7] E. N. K. Cressman, M. M. Shenoi, T. L. Edelman, M. G. Geeslin, L. J. Hennings, Y. Zhang, P. A. Iaizzo, and J. C. Bischof, "In vivo comparison of simultaneous versus sequential injection technique for thermochemical ablation in a porcine model," *Int. J. Hyperth. Off. J. Eur. Soc. Hyperthermic Oncol. North Am. Hyperth. Group*, vol. 28, no. 2, pp. 105–112, 2012.

[8] S. N. Goldberg, "Radiofrequency tumor ablation: principles and techniques," *Eur. J. Ultrasound Off. J. Eur. Fed. Soc. Ultrasound Med. Biol.*, vol. 13, no. 2, pp. 129–147, Jun. 2001.

[9] C. M. Pacella, G. Francica, and G. G. Di Costanzo, "Laser Ablation for Small Hepatocellular Carcinoma," *Radiol. Res. Pract.*, vol. 2011, p. e595627, Dec. 2011.

[10] G. Shafirstein, Y. Kaufmann, L. Hennings, E. Siegel, R. J. Griffin, P. Novák, S. Ferguson, and E. G. Moros, "Conductive interstitial thermal therapy (CITT) inhibits recurrence and metastasis in rabbit VX2 carcinoma model," *Int. J. Hyperth. Off. J. Eur. Soc. Hyperthermic Oncol. North Am. Hyperth. Group*, vol. 25, no. 6, pp. 446–454, 2009.

[11] Y.-F. Zhou, "High intensity focused ultrasound in clinical tumor ablation," *World J. Clin. Oncol.*, vol. 2, no. 1, pp. 8–27, Jan. 2011.

[12] R. H. De Gouveia, J. Melo, T. Santiago, and A. P. Martins, "Comparison of the Healing Mechanisms of Myocardial Lesions Induced by Dry Radiofrequency and Microwave Epicardial Ablation," *Pacing Clin. Electrophysiol.*, vol. 29, no. 3, pp. 278–282, Mar. 2006.

[13] G. Shafirstein, P. Novák, E. G. Moros, E. Siegel, L. Hennings, Y. Kaufmann, S. Ferguson, J. Myhill, M. Swaney, and P. Spring, "Conductive interstitial thermal therapy device for surgical margin ablation: in vivo verification of a theoretical model," *Int. J. Hyperth. Off. J. Eur. Soc. Hyperthermic Oncol. North Am. Hyperth. Group*, vol. 23, no. 6, pp. 477–492, Sep. 2007.

[14] M. R. Williams, M. Knaut, D. Bérubé, and M. C. Oz, “Application of microwave energy in cardiac tissue ablation: from in vitro analyses to clinical use,” *Ann. Thorac. Surg.*, vol. 74, no. 5, pp. 1500–1505, Nov. 2002.
[15] C. Rappaport, “Cardiac tissue ablation with catheter-based microwave heating,” *Int. J. Hyperthermia*, vol. 20, no. 7, pp. 769–780, Jan. 2004.
[16] C. L. Brace, “Radiofrequency and Microwave Ablation of the Liver, Lung, Kidney, and Bone: What Are the Differences?,” *Curr. Probl. Diagn. Radiol.*, vol. 38, no. 3, pp. 135–143, May 2009.
[17] C. Pusceddu, B. Sotgia, R. M. Fele, and L. Melis, “Treatment of bone metastases with microwave thermal ablation,” *J. Vasc. Interv. Radiol. JVIR*, vol. 24, no. 2, pp. 229–233, Feb. 2013.
[18] Y. Lin, P. Liang, X. Yu, J. Yu, Z. Cheng, Z. Han, and F. Liu, “Percutaneous microwave ablation of renal cell carcinoma is safe in patients with a solitary kidney,” *Urology*, vol. 83, no. 2, pp. 357–363, Feb. 2014.
[19] E. S. Alexander and D. E. Dupuy, “Lung cancer ablation: technologies and techniques,” *Semin. Interv. Radiol.*, vol. 30, no. 2, pp. 141–150, Jun. 2013.
[20] J. M. Bertram, D. Yang, M. C. Converse, J. G. Webster, and D. M. Mahvi, “A review of coaxial-based interstitial antennas for hepatic microwave ablation,” *Crit. Rev. Biomed. Eng.*, vol. 34, no. 3, pp. 187–213, 2006.
[21] H. Zhang, Q. Nan, and Y. Liu, “SAR distribution of microwave antenna for atrial fibrillation catheter ablation,” in *2012 5th International Conference on Biomedical Engineering and Informatics (BMEI)*, 2012, pp. 664–667.
[22] J. Hand, in *Physics of Thermal Therapy: Fundamentals and Clinical Applications*, CRC Press, 2013, pp. 57–74.
[23] M. W. Dewhirst, in *Physics of Thermal Therapy: Fundamentals and Clinical Applications*, CRC Press, 2013, pp. 279–318.
[24] C. A. Balanis, *Advanced Engineering Electromagnetics*. Harper and Row, 1982.
[25] “IEEE Standard Definitions of Terms for Radio Wave Propagation,” *IEEE Std 211-1997*, p. i–, 1998.
[26] J. A. Pearce, J. R. Cook, and S. Y. Emelianov, “Ferrimagnetic nanoparticles enhance microwave heating for tumor hyperthermia therapy,” in *2010 Annual International Conference of the IEEE Engineering in Medicine and Biology Society (EMBC)*, 2010, pp. 2751–2754.
[27] M. G. Lubner, C. L. Brace, J. L. Hinshaw, and F. T. Lee Jr, “Microwave Tumor Ablation: Mechanism of Action, Clinical Results, and Devices,” *J. Vasc. Interv. Radiol.*, vol. 21, no. 8, Supplement, pp. S192–S203, Aug. 2010.
[28] R. Tarkowski and M. Rzaca, “Cryosurgery in the treatment of women with breast cancer-a review,” *Gland Surg.*, vol. 3, no. 2, pp. 88–93, May 2014.
[29] R. D. Tucker, C. E. Platz, C. Huidobro, and T. Larson, “Interstitial thermal therapy in patients with localized prostate cancer: histologic analysis,” *Urology*, vol. 60, no. 1, pp. 166–169, Jul. 2002.
[30] D. Kitchin, M. Lubner, T. Ziemlewicz, J. L. Hinshaw, M. Alexander, C. L. Brace, and F. Lee, “Microwave ablation of malignant hepatic tumours: Intraperitoneal fluid instillation prevents collateral damage and allows more aggressive case selection,” *Int. J. Hyperthermia*, vol. 30, no. 5, pp. 299–305, Aug. 2014.

[31] R. C. Ward, T. T. Healey, and D. E. Dupuy, “Microwave ablation devices for interventional oncology,” *Expert Rev. Med. Devices*, vol. 10, no. 2, pp. 225–238, Mar. 2013.
[32] J. M. Bertram, D. Yang, M. C. Converse, J. G. Webster, and D. M. Mahvi, “A review of coaxial-based interstitial antennas for hepatic microwave ablation,” *Crit. Rev. Biomed. Eng.*, vol. 34, no. 3, pp. 187–213, 2006.
[33] T. P. Ryan, P. F. Turner, and B. Hamilton, “Interstitial microwave transition from hyperthermia to ablation: historical perspectives and current trends in thermal therapy,” *Int. J. Hyperth. Off. J. Eur. Soc. Hyperthermic Oncol. North Am. Hyperth. Group*, vol. 26, no. 5, pp. 415–433, 2010.
[34] P. Prakash, M. C. Converse, J. G. Webster, and D. M. Mahvi, “An Optimal Sliding Choke Antenna for Hepatic Microwave Ablation,” *IEEE Trans. Biomed. Eng.*, vol. 56, no. 10, pp. 2470–2476, Oct. 2009.
[35] D. Berube and J. Gauthier, “Microwave ablation instrument with a directional radiation pattern,” US6471696 B1, 29-Oct-2002.
[36] S. D. Edwards, J. Jackson, R. A. Stern, T. M. Morse, and P. M. Owens, “Steerable antenna systems for cardiac ablation that minimize tissue damage and blood coagulation due to conductive heating patterns,” US5281217 A, 25-Jan-1994.
[37] P. S. Debicki, M. Okoniewski, E. Okoniewska, P. N. Shrivastava, A. M. Debicka, L. V. Baert, and Z. Petrovich, “Cooled microwave transrectal applicator with adjustable directional beam for prostate treatment,” *Int. J. Hyperth. Off. J. Eur. Soc. Hyperthermic Oncol. North Am. Hyperth. Group*, vol. 11, no. 1, pp. 95–108, Feb. 1995.
[38] R. Chopra, M. J. Bronskill, and F. S. Foster, “Feasibility of linear arrays for interstitial ultrasound thermal therapy,” *Med. Phys.*, vol. 27, no. 6, pp. 1281–1286, Jun. 2000.
[39] C. J. Diederich, R. J. Stafford, W. H. Nau, E. C. Burdette, R. E. Price, and J. D. Hazle, “Transurethral ultrasound applicators with directional heating patterns for prostate thermal therapy: in vivo evaluation using magnetic resonance thermometry,” *Med. Phys.*, vol. 31, no. 2, pp. 405–413, Feb. 2004.
[40] K. Shinohara, “Thermal ablation of prostate diseases: advantages and limitations,” *Int. J. Hyperthermia*, vol. 20, no. 7, pp. 679–697, Jan. 2004.
[41] H. Rhim, G. D. Dodd, K. N. Chintapalli, B. J. Wood, D. E. Dupuy, J. L. Hvizda, P. E. Sewell, and S. N. Goldberg, “Radiofrequency thermal ablation of abdominal tumors: lessons learned from complications,” *Radiogr. Rev. Publ. Radiol. Soc. N. Am. Inc*, vol. 24, no. 1, pp. 41–52, Feb. 2004.
[42] F. Izzo, R. Thomas, P. Delrio, M. Rinaldo, P. Vallone, A. DeChiara, G. Botti, G. D’Aiuto, P. Cortino, and S. A. Curley, “Radiofrequency ablation in patients with primary breast carcinoma,” *Cancer*, vol. 92, no. 8, pp. 2036–2044, 2001.
[43] C. Gabriel, S. Gabriel, E. H. Grant, E. H. Grant, B. S. J. Halstead, and D. Michael P. Mingos, “Dielectric parameters relevant to microwave dielectric heating,” *Chem. Soc. Rev.*, vol. 27, no. 3, p. 213, 1998.
[44] S. Gabriel, R. W. Lau, and C. Gabriel, “The dielectric properties of biological tissues: III. Parametric models for the dielectric spectrum of tissues,” *Phys. Med. Biol.*, vol. 41, no. 11, p. 2271, Nov. 1996.
[45] S. Tungjitkusolmun, E. J. Woo, H. Cao, J. Z. Tsai, V. R. Vorperian, and P. J. G. Webster, “Thermal—electrical finite element modelling for radio frequency cardiac ablation: Effects of changes in myocardial properties,” *Med. Biol. Eng. Comput.*, vol. 38, no. 5, pp. 562–568, Sep. 2000.

[46] D. Haemmerich, L. Chachati, A. S. Wright, D. M. Mahvi, F. T. Lee, and J. G. Webster, "Hepatic radiofrequency ablation with internally cooled probes: effect of coolant temperature on lesion size," *IEEE Trans. Biomed. Eng.*, vol. 50, no. 4, pp. 493–500, Apr. 2003.
[47] P. Prakash and C. J. Diederich, "Considerations for theoretical modelling of thermal ablation with catheter-based ultrasonic sources: implications for treatment planning, monitoring and control," *Int. J. Hyperth. Off. J. Eur. Soc. Hyperthermic Oncol. North Am. Hyperth. Group*, vol. 28, no. 1, pp. 69–86, 2012.
[48] C. Chan, F. Lam, and R. Rohling, "A needle tracking device for ultrasound guided percutaneous procedures," *Ultrasound Med. Biol.*, vol. 31, no. 11, pp. 1469–1483, Nov. 2005.
[49] E. B. Levy, J. Tang, D. Lindisch, N. Glossop, F. Banovac, and K. Cleary, "Implementation of an Electromagnetic Tracking System for Accurate Intrahepatic Puncture Needle Guidance: Accuracy Results in an In Vitro Model," *Acad. Radiol.*, vol. 14, no. 3, pp. 344–354, Mar. 2007.
[50] F. Banovac, N. Glossop, D. Lindisch, D. Tanaka, E. Levy, and K. Cleary, "Liver Tumor Biopsy in a Respiring Phantom with the Assistance of a Novel Electromagnetic Navigation Device," in *Medical Image Computing and Computer-Assisted Intervention — MICCAI 2002*, T. Dohi and R. Kikinis, Eds. Springer Berlin Heidelberg, 2002, pp. 200–207.
[51] P. Wust, B. Hildebrandt, G. Sreenivasa, B. Rau, J. Gellermann, H. Riess, R. Felix, and P. Schlag, "Hyperthermia in combined treatment of cancer," *Lancet Oncol.*, vol. 3, no. 8, pp. 487–497, Aug. 2002.
[52] J. van der Zee, D. González, G. C. van Rhoon, J. D. van Dijk, W. L. van Putten, and A. A. Hart, "Comparison of radiotherapy alone with radiotherapy plus hyperthermia in locally advanced pelvic tumours: a prospective, randomised, multicentre trial," *The Lancet*, vol. 355, no. 9210, pp. 1119–1125, Apr. 2000.
[53] O. Dahl, R. Dalene, B. C. Schem, and O. Mella, "Status of Clinical Hyperthermia," *Acta Oncol.*, vol. 38, no. 7, pp. 863–873, Nov. 1999.
[54] B. Hildebrandt and P. Wust, "The biologic rationale of hyperthermia," *Cancer Treat. Res.*, vol. 134, pp. 171–184, 2007.
[55] P. Wust, B. Hildebrandt, G. Sreenivasa, B. Rau, J. Gellermann, H. Riess, R. Felix, and P. Schlag, "Hyperthermia in combined treatment of cancer," *Lancet Oncol.*, vol. 3, no. 8, pp. 487–497, Aug. 2002.
[56] C.-K. Chou, "Application of electromagnetic energy in cancer treatment," *IEEE Trans. Instrum. Meas.*, vol. 37, no. 4, pp. 547–551, Dec. 1988.
[57] P. Wust, B. Hildebrandt, G. Sreenivasa, B. Rau, J. Gellermann, H. Riess, R. Felix, and P. Schlag, "Hyperthermia in combined treatment of cancer," *Lancet Oncol.*, vol. 3, no. 8, pp. 487–497, Aug. 2002.
[58] F. Sterzer, R. W. Paglione, J. Mendecki, E. Friedenthal, and C. Botstein, "Electronics in medicine: RF therapy for malignancy: Heating of malignant tissues (hyperthermia) by RF radiation presents a new tool in the arsenal of weapons against cancer," *IEEE Spectr.*, vol. 17, no. 12, pp. 32–37, Dec. 1980.
[59] J. C. Lin and Y. J. Wang, "Interstitial microwave antennas for thermal therapy," *Int. J. Hyperth. Off. J. Eur. Soc. Hyperthermic Oncol. North Am. Hyperth. Group*, vol. 3, no. 1, pp. 37–47, Feb. 1987.

[60] R. B., J. Gellermann, J. Nadobny, P. Wust M. Seebass, “Electromagnetic phased arrays for regional hyperthermia: optimal frequency and antenna arrangement,” *Int. J. Hyperthermia*, vol. 17, no. 4, pp. 321–336, Jan. 2001.
[61] Z. Petrovich, B. Emami, M. Astrahan, B. Langholz, and G. Luxton, “Regional hyperthermia with BSD-1000 annular phased array in the management of recurrent deep seated malignant tumors,” *Strahlenther. Onkol. Organ Dtsch. Röntgenges. Al*, vol. 163, no. 7, pp. 430–433, Jul. 1987.
[62] P. R. Stauffer, F. Rossetto, M. Prakash, D. G. Neuman, and T. Lee, “Phantom and animal tissues for modelling the electrical properties of human liver,” *Int. J. Hyperth. Off. J. Eur. Soc. Hyperthermic Oncol. North Am. Hyperth. Group*, vol. 19, no. 1, pp. 89–101, Feb. 2003.
[63] A. P. O’Rourke, M. Lazebnik, J. M. Bertram, M. C. Converse, S. C. Hagness, J. G. Webster, and D. M. Mahvi, “Dielectric properties of human normal, malignant and cirrhotic liver tissue: in vivo and ex vivo measurements from 0.5 to 20 GHz using a precision open-ended coaxial probe,” *Phys. Med. Biol.*, vol. 52, no. 15, pp. 4707–4719, Aug. 2007.
[64] W. T. Joines, Y. Zhang, C. Li, and R. L. Jirtle, “The measured electrical properties of normal and malignant human tissues from 50 to 900 MHz,” *Med. Phys.*, vol. 21, no. 4, pp. 547–550, Apr. 1994.
[65] A. Mashal, B. Sitharaman, X. Li, P. K. Avti, A. V. Sahakian, J. H. Booske, and S. C. Hagness, “Toward Carbon-Nanotube-Based Theranostic Agents for Microwave Detection and Treatment of Breast Cancer: Enhanced Dielectric and Heating Response of Tissue-Mimicking Materials,” *IEEE Trans. Biomed. Eng.*, vol. 57, no. 8, pp. 1831–1834, Aug. 2010.
[66] J. A. Pearce, J. R. Cook, and S. Y. Emelianov, “Ferrimagnetic nanoparticles enhance microwave heating for tumor hyperthermia therapy,” in *2010 Annual International Conference of the IEEE Engineering in Medicine and Biology Society (EMBC)*, 2010, pp. 2751–2754.
[67] A. Mashal, B. Sitharaman, X. Li, P. K. Avti, A. V. Sahakian, J. H. Booske, and S. C. Hagness, “Toward Carbon-Nanotube-Based Theranostic Agents for Microwave Detection and Treatment of Breast Cancer: Enhanced Dielectric and Heating Response of Tissue-Mimicking Materials,” *IEEE Trans. Biomed. Eng.*, vol. 57, no. 8, pp. 1831–1834, Aug. 2010.
[68] D. Haemmerich, D. J. Schutt, I. dos Santos, J. G. Webster, and D. M. Mahvi, “Measurement of temperature-dependent specific heat of biological tissues,” *Physiol. Meas.*, vol. 26, no. 1, p. 59, Feb. 2005.
[69] A. M. Elliott, A. M. Shetty, J. Wang, J. D. Hazle, and R. Jason Stafford, “Use of gold nanoshells to constrain and enhance laser thermal therapy of metastatic liver tumours,” *Int. J. Hyperthermia*, vol. 26, no. 5, pp. 434–440, Jul. 2010.